AD A140025

RADC-TR-83-261, Vol I (of two)
Interim Report
December 1983

ACOSS ELEVEN (ACTIVE CONTROL OF SPACE STRUCTURES)

The Charles Stark Draper Laboratory, Inc.

APPROVED FOR PUBLIC RELEASE; DISTRIBUTION UNLIMITED

DTIC FILE COPY

ROME AIR DEVELOPMENT CENTER
Air Force Systems Command
Griffiss Air Force Base, NY 13441

DTIC
ELECTE
APR 1 1 1984
D

84 04 11 004

This report has been reviewed by the RADC Public Affairs Office (PA) and is releasable to the National Technical Information Service (NTIS). At NTIS it will be releasable to the general public, including foreign nations.

RADC-TR-83-261, Vol I (of two) has been reviewed and is approved for publication.
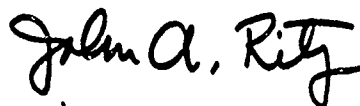
APPROVED: *Richard W. Carman*

RICHARD W. CARMAN
Project Engineer

APPROVED: *Frank J. Rehm*

FRANK J. REHM
Technical Director
Surveillance Division

FOR THE COMMANDER: *John A. Ritz*

JOHN A. RITZ
Acting Chief, Plans Office

ACOSS ELEVEN (ACTIVE CONTROL OF SPACE STRUCTURES)
Vol I

Thomas H. Brooks Glen J. Kissel

Virendran Mahajan Harris N. McClamroch

Daniel R. Hegg James D. Turner

REPORT DOCUMENTATION PAGE	READ INSTRUCTIONS BEFORE COMPLETING FORM
1. REPORT NUMBER RADC-TR-83-261, Vol I (of two) **2. GOVT ACCESSION NO.** AD-A140025	**3. RECIPIENT'S CATALOG NUMBER**
4. TITLE *(and Subtitle)* ACOSS ELEVEN (ACTIVE CONTROL OF SPACE STRUCTURES)	**5. TYPE OF REPORT & PERIOD COVERED** Interim Report Nov 82 – May 83
	6. PERFORMING ORG. REPORT NUMBER CSDL-R-1648
7. AUTHOR(s) Thomas H. Brooks Glen J. Kissel Virendran Mahajan Harris N. McClamroch Daniel R. Hegg James D. Turner	**8. CONTRACT OR GRANT NUMBER(s)** F30602-81-C-0180
9. PERFORMING ORGANIZATION NAME AND ADDRESS The Charles Stark Draper Laboratory, Inc. 555 Technology Square Cambridge MA 02139	**10. PROGRAM ELEMENT, PROJECT, TASK AREA & WORK UNIT NUMBERS** 62301E C6550104
11. CONTROLLING OFFICE NAME AND ADDRESS Defense Advanced Research Projects Agency 1400 Wilson Blvd Arlington VA 22209	**12. REPORT DATE** December 1983
	13. NUMBER OF PAGES 64
14. MONITORING AGENCY NAME & ADDRESS(*If different from Controlling Office*) Rome Air Development Center (OCSE) Griffiss AFB NY 13441	**15. SECURITY CLASS.** *(of this report)* UNCLASSIFIED
	15a. DECLASSIFICATION/DOWNGRADING SCHEDULE N/A

16. DISTRIBUTION STATEMENT *(of this Report)*

Approved for public release; distribution unlimited

17. DISTRIBUTION STATEMENT *(of the abstract entered in Block 20, if different from Report)*

Same

18. SUPPLEMENTARY NOTES

RADC Project Engineer: Richard W. Carman (OCSE)

19. KEY WORDS *(Continue on reverse side if necessary and identify by block number)*

Draper Integrated Simulations	Deconvolution
Space-Based IR Surveillance Systems	Active Mirrors
Infrared Terrestrial Scene Simulation	Mirror Deformations
Line-of-Sight Stabilization	Wavefront Errors
Clutter Leakage	Ray Tracing

20. ABSTRACT *(Continue on reverse side if necessary and identify by block number)*

Simulation Extension: The overall objective of the Simulation Extensions project is to identify and quantify those generic mission, scenario and sensor parameters (as well as their interactions) which drive the performance of space-based staring IR surveillance systems. The approach taken to achieve this overall objective has proceeded along two main avenues; Simulation Enhancements, and Simulation Applications.

Efforts in the Simulation Enhancements area are directed toward generali-

DD FORM 1 JAN 73 **1473**   EDITION OF 1 NOV 65 IS OBSOLETE

zing those models in the Draper Integrated Simulations (DIS) which are too limited in scope or perhaps restricted to one particular system. In support of the Simulation Enhancements effort, work has been performed (or is in progress) on models for the platform, sensor (including focal plane and signal processor), and scene. The status of these efforts is summarized.

Utilizing the tools developed as a result of the Simulation Enhancements work, the Simulation Applications effort studies issues related to generic surveillance system performance drivers. Results are reported from a study which examines the effects of spectral band selection and scene local time of day on line-of-sight jitter-induced clutter leakage through the signal processor of a generic surveillance system.

Halo Optics: CSDL prepared a deconvolution test to validate Itek's deconvolution algorithm for correcting a deformed HALO optical system. The algorithm uses the wavefront errors measured by a wavefront sensor to determine the actuator signals. This report describes a limited blind test and concludes that the algorithm successfully determined the actuator displacements from the wavefront errors provided in this test. Recommendations for a more complete test are outlined.

TABLE OF CONTENTS

ACKNOWLEDGEMENT

INTRODUCTION

1.1 Simulation Extensions

The objective of this project is to identify and quantify those generic mission, scenario and sensor parameters (as well as their interactions) which drive the performance of space-based staring IR surveillance systems. These efforts have been divided into two efforts: Simulation Enhancements; and Simulation Applications.

Work in the Simulation Enhancements area is directed toward generalizing those models in the Draper Integrated Simulations (DIS) which are too limited in scope or perhaps restricted to one particular system. Models have been prepared for the platform, sensor (including focal plane and signal processor), scene, and techniques for interfacing the DIS with an in-house image processor for graphics display.

The Simulation Applications effort studies issues related to generic surveillance system performance drivers using tools from the Simulation Enhancement effort. Typical examples are sensor line-of-sight stability, focal D^*, and critical scene/scenario characteristics.

1.2 HALO Optics

HALO is a multi-mirror large optical imaging system with a wide field of view. To maintain alignment as well as image quality, the mirrors are actively controlled with actuators. The term "deconvolution" implies a sensing and control scheme by which a deformed HALO optical system is corrected in near real time. In one of the techniques worked on by the Itek Corporation, the wavefront errors of the deformed system are measured with a wavefront sensor for several object points near the edge of the field-of-view of the system. The wavefront sensor is placed around the focal plane. The wavefront errors are decomposed into mirror figure errors and actuator displacements are generated to correct them with a deconvolution algorithm. This report describes a limited blind test that CSDL prepared for Itek to test and validate this algorithm. We conclude that the algorithm successfuly determined the actuator displacements from the wavefront errors considered in this test. The residual wavefront errors were negligibly small and below the wavefront sensor noise.

It is recommended that one more blind test be prepared for Itek's deconvolution algorithm to include more realism. Some of the desirable features of this test are listed below.

1) Mirror deformations will not be produced by the actuators used for correction, because, in practice, a mirror is not deformed by the movement of actuators.

2) Some static aberrations will be added to the optical system to simulate a nondiffraction-limited undeformed system.

3) The on-axis wavefront error data may not be excluded, since the wavefront sensor placed around the HALO focal plane cannot sense it.

4) The actuator influence functions used for mirror figure correction will be slightly different from those used by Itek in their algorithm, to simulate errors in the knowledge of influence function.

5) The influence function for edge actuators may be different from that for interior actuators.

SIMULATION EXTENSIONS PROJECT

2.1   Introduction

The overall objective of this project is to identify and quantify those generic mission, scenario and sensor parameters (as well as their interactions) which drive the performance of space-based staring IR surveillance systems. The approach taken to achieve this overall objective has proceeded along two main avenues: Simulation Enhancements; and Simulation Applications.

Efforts in the Simulation Enhancements area are directed toward generalizing those models in the Draper Integrated Simulations (DIS) which are too limited in scope or perhaps restricted to one particular system. Figure 2-1 presents a simplified block diagram of the DIS. In support of the Simulation Enhancements effort, work has been performed (or is in progress) on models for the platform, sensor (including focal plane and signal processor), scene, and techniques for interfacing the DIS with an in-house image processor for graphics display.

Utilizing the tools developed as a result of the Simulation Enhancements work, the Simulation Applications effort studies issues related to generic surveillance system performance drivers. Typical examples are sensor line-of-sight stability, focal D^*, and critical scene/scenario characteristics such as spectral interval, orbit, scene time-of-day, etc.

2.2   Simulation Enhancements

2.2.1   Platform Simulation

Development of the Integrated Large Space Structures Simulation (ILS^3) was begun in 1977 in response to a DARPA need for simulating the optical performance of the HALO system. While intended to be general purpose, the internal structure of the ILS^3 (i.e., input, coordinate systems, interpolation methods, contact systems, etc.) was rigidly based on the HALO design. More recently, many analysis efforts have concentrated on single reflector or feedreflector systems. In the absence of a suitable raytrace program to provide the necessary inputs for utilizing the ILS^3, alternate special-purpose software packages were developed which did not require a raytrace and which could compute wavefront errors for these simple paraboloidal or spherical systems. While these software packages were adequate for their intended purposes, this approach has three major disadvantages: the packages are problem-specific and must be modified, sometimes extensively, for other applications; no linkage with the DIS is provided; and documentation tends to be scattered and incomplete.

The purpose of the enhancements to the ILS^3 is to assemble a package which can be used to analyze both multi-mirror raytraced systems and single surface, paraboloidal or spherical systems. This is being done in five steps: incorporating many of the previously proposed ILS^3 changes; incorporating a

Figure 2-1. DIS block diagram.
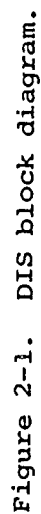
general purpose version of the single mirror software; adding a compatible raytrace program; simplifying data communication; and providing linkage to the NASTRAN and DISCOS programs. The use of NASTRAN is important both to provide input to the top level ILS[3] modules (dynamics, steady-state, and quasistatic) and in many cases to serve as a replacement for them. These enhancements will provide significant new capabilities for dealing with both infrared and radar systems.

An initial plan has been formulated and preliminary analysis completed to accomplish the above objectives. The remainder of this effort is currently in process.

2.2.2 Sensor Simulation

Many aspects of the focal plane and signal processor models originally in the DIS were specific to the Mini-HALO system. In order to be able to study effectively the capabilities of a generic space-based staring infrared surveillance system, it was necessary to generalize certain aspects of each of these models.

The principal enhancement to the focal plane model was to implement a menu of user-selectable noise models. In addition to the standard noise model corresponding to the basic Mini-HALO focal plane (including saturation and reset features), the user may select that of an ideal focal plane (i.e., scene shot noise only) or may specify either D^* or D^*/D^*_{BLIP} to characterize focal plane noise. In the latter case the user may further specify either a white noise or 1/f noise spectrum.

The initial signal processor model in the DIS corresponded to the HALO Signal Processor (HSP). To increase flexibility and modularity, the software architecture for the Signal Processor has been restructured, leaving intact, however, the core HSP algorithm chain. In order to be able to deal with the needs of a general class of space-based staring IR surveillance systems, the character of many of these algorithms has been parameterized, and a number of new algorithms have been added. The focus of much of this activity has been in the following areas: target signature templates; thresholding procedures; threshold level computation and scaling; and "system track" and "acquired track" criteria.

The Sensor Simulation Enhancements are complete at this point and now being used in DIS applications.

2.2.3 Scene Simulation

The single most important initiative undertaken in the Simulation Extensions Project has been the development of an in-house generic scene simulation in order to bring within the scope of the DIS the capability to generate, manipulate and analyze terrestrial scene data sets as functions of the major surveillance system, scenario and mission parameters. This effort has been accomplished by working in conjunction with Photon Research Associates (PRA). Under subcontract to CSDL, PRA is developing a software simulation called GENESSIS to meet DIS needs for scene generation and manipulation. The

PRA work is proceeding in two phases: GENESSIS-I, to provide a near-term capability with certain simplifying assumptions and a limited scene data base; and GENESSIS-II, in which all critical scene parameters will be modelled and automated access provided to the DMA/Landsat data base to enable generation of scenes corresponding to any region for which DMA (Defense Mapping Agency) data exists. Tables 2-1 and 2-2 provide a summary of the principal features and current status of GENESSIS-I and GENESSIS-II, respectively. Figure 2-2 presents a simplified block diagram of the GENESSIS software architecture.

2.3   Simulation Applications

The Simulation Enhancements described above have considerably expanded the scope and capability of the DIS to conduct end-to-end performance assessments of space-based staring infrared surveillance systems. As an illustration of this new capability, the DIS has been used to study the effect of choice of spectral interval and selection of scene local time of day on clutter leakage through the signal processor. The basic approach was to begin with the California coast (Santa Cruz) data base and to use GENESSIS to produce two scenes in the 3.6-4.0 µm band and two scenes in the 8.0-9.0 µm band, each pair of scenes corresponding to 8 AM and to noon local time, respectively. A nominal surveillance system mission and configuration were assumed, and the above scenes were processed through the DIS under varying levels of line-of-sight (LOS) jitter. Tables 2-3 and 2-4 summarize the scenario, sensor and signal processor configurations for this investigation. These parameter values reflect the basic configuration for a system whose principal objective is the detection of strategic aircraft against a terrestrial background. The figure of merit used to measure clutter leakage in the signal processor was average number of threshold exceedances per frame. Figure 2-3 illustrates the four scenes used. The spectrum at the bottom of the figure indicates relative temperature (or scene radiance) within each scene.

Since the average number of threshold exceedances per frame is a function of threshold level in the signal processor as well as the level of LOS jitter, the results of this study may be presented from those two points of view. Figure 2-4 shows the dependence on LOS jitter level of the average number of threshold exceedances per frame. The particular threshold level selected is representative of what would be used to acquire a target with a relatively high signal-to-noise ratio. The general trend of the data is such that, for a given level of LOS jitter, higher numbers of exceedances are found in the LWIR band (i.e., 8.0-9.0 µm) than in the SWIR band (i.e., 3.6-4.0 µm). In either band, the higher number of exceedances always occurs at noon local time as opposed to 8 AM.

Figures 2-5 through 2-7 show the dependence of average number of threshold exceedances per frame on threshold level, for progressively increasing values of LOS jitter. Many of the same trends are also evident in this data. Decreasing the threshold results in a rapid increase in threshold exceedances. At a given threshold value, higher numbers of threshold exceedances always occur in the LWIR band as opposed to the SWIR, and, within each band higher numbers of exceedances occur at noon in comparison with 8 AM. Increasing the LOS jitter level results in a translation upward of the curves at higher

6

Table 2-1. Generic scene simulation Phase I (GENESSIS-I).

FEATURES

• User-specified variables

    -Observer altitude, zenith angle
    -Spectral interval (2.5-13.0 μm)
    -Atmospheric model (LOWTRAN)
    -Field-of-view location (within overall scene)
    -Scene angular resolution

• Five representative terrain data bases

    -California Coast (near Santa Cruz)
    -Brooks Range Mountains of Alaska
    -Arctic Tundra
    -Middle Fast
    -Central Europe

• Each data base topology extracted from DMA data base

• Each data base registered with Landsat data to obtain materials assignments

    -Limited to 14 material types

• Two representative cloud templates (for superposition over terrain data bases)

• Scene size: 40 km × 40 km

STATUS

• Operational at CSDL

Table 2-2. Generic scene simulation Phase II (GENESSIS-II).

FEATURES

• Enhanced data base

  -Material types expanded to 20
  -Geometrical representations for three additional cloud
   patterns (Derived from NOAA data)

• GENESSIS/DMA-Landsat interface

  -Software package to automate generation of input data bases
   from raw DMA and Landsat data
  -Will permit generation of any scenes for which DMA data
   exists

• Generalized treatment of key atmospheric effects

  -Continuously variable surface-level parameters (e.g.,
   temperature, humidity, wind velocity, skyshine, solar
   scattering)

• Optimized software architecture

• Detailed user's manual

STATUS

• GENESSIS-II (Part 1) subcontract to PRA currently underway
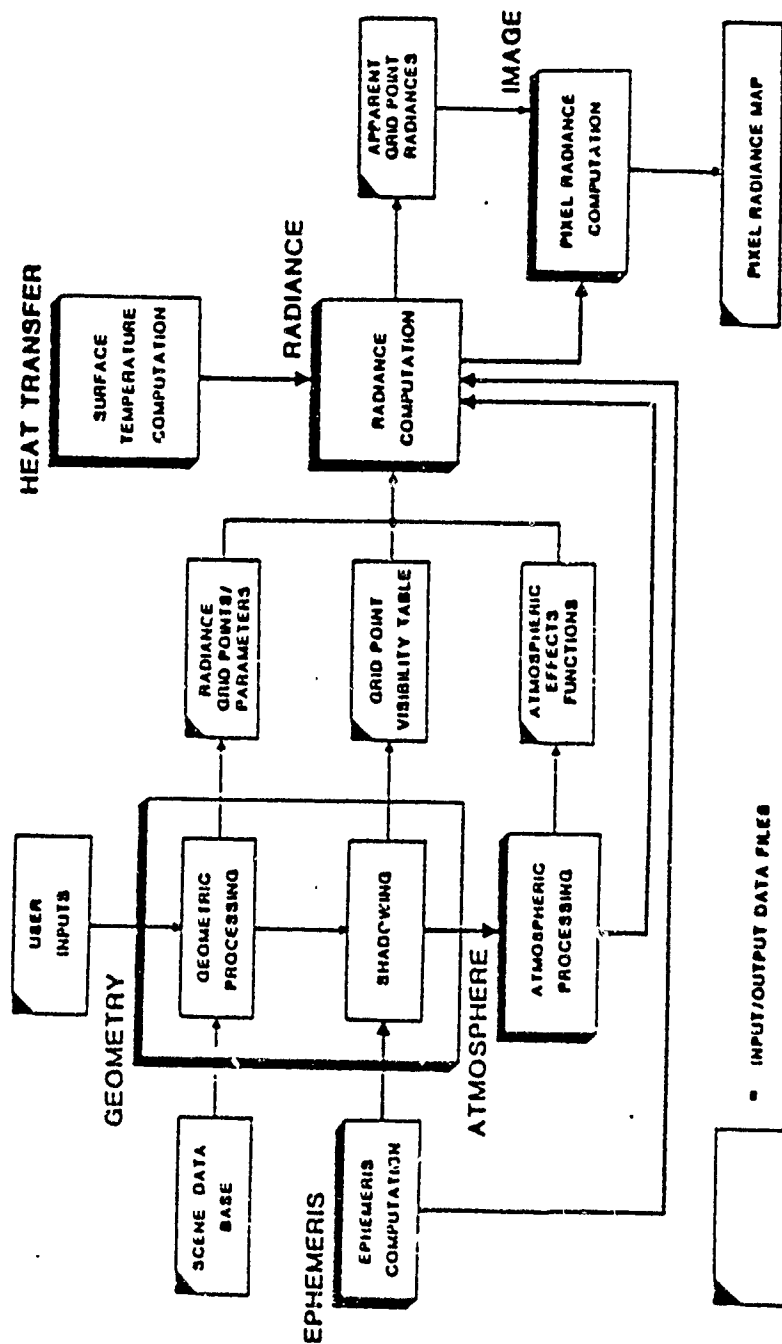
Figure 2-2. GENESSIS software architecture simplified block diagram.

9

Table 2-3. Scenario and sensor specification for GENESSIS Santa Cruz investigation.

PARAMETER	VALUE
Target	None
Backgrounds	
-Location	Santa Cruz (GENESSIS)
-Spectral Bands	3.6-4.0 μm 8.0-9.0 μm
-Times of Day (Local)	8 AM NOON
Spacecraft	
-Drift	None
-Jitter	0.1 μrad rms 0.5 μrad rms 1.0 μrad rms
-Altitude	35,700 km
-Boresight	NADIR
Optics	
-Aperture Diameter	1.4 m
-Obscuration Ratio	0.35
-Thruput	0.135
-Point-spread Function	Gaussian ($\sigma = 5.01$ μrad)
Focal Plane	
-Detector Geometry	25 × 25 Array of 100 μm (20 μrad) Square Pixels
-Frame Duration	3.4 sec
-D*	2.8 $(10)^{12}$ cm $\sqrt{Hz}$/W
-Responsivity non-uniformity	
.Fixed Pattern	0%
.Random	15%

Table 2-4. Signal processor configuration for GENESSIS
Santa Cruz investigation.

PARAMETER	VALUE
Difference Filter	3rd Order
Threshold Level	User Input
Assumed Target Contrast	Negative
Threshold Templates	CSDL MTD
Threshold Algorithm	CSDL Rationalized Exceedance Thresholding (Version 1)
Cluster Basis	Threshold Exceedances
Centroid Basis	Threshold Exceedances
System Track Criterion	3 out of 3
Acquired Track Criterion	10 out of 12
System Track Threshold Scaling	0.5
Least Squares Track Linearity Criterion	±1.8 Pixels

3.6–4.0 μm
NOON

8.0–9.0 μm
NOON

3.6–4.0 μm
8 AM

8.0–9.0 μm
8 AM

Figure 2-3. Composite of GENESSIS Santa Cruz scenes.

12

Figure 2-4. Average clutter leakage as a function of line-of-sight jitter level for the GENESSIS Santa Cruz scene, with local time-of-day and spectral band as parameters.

Figure 2-5. Average clutter leakage as a function of threshold level for the GENESSIS Santa Cruz scene, with local time of day and spectral band as parameters. (LOS Jitter = 0.1 μrad RMS)

14

Figure 2-6. Average clutter leakage as a function of threshold level for the GENESSIS Santa Cruz scene with local time of day and spectral band as parameters. (LOS Jitter = 0.5 μrad RMS)

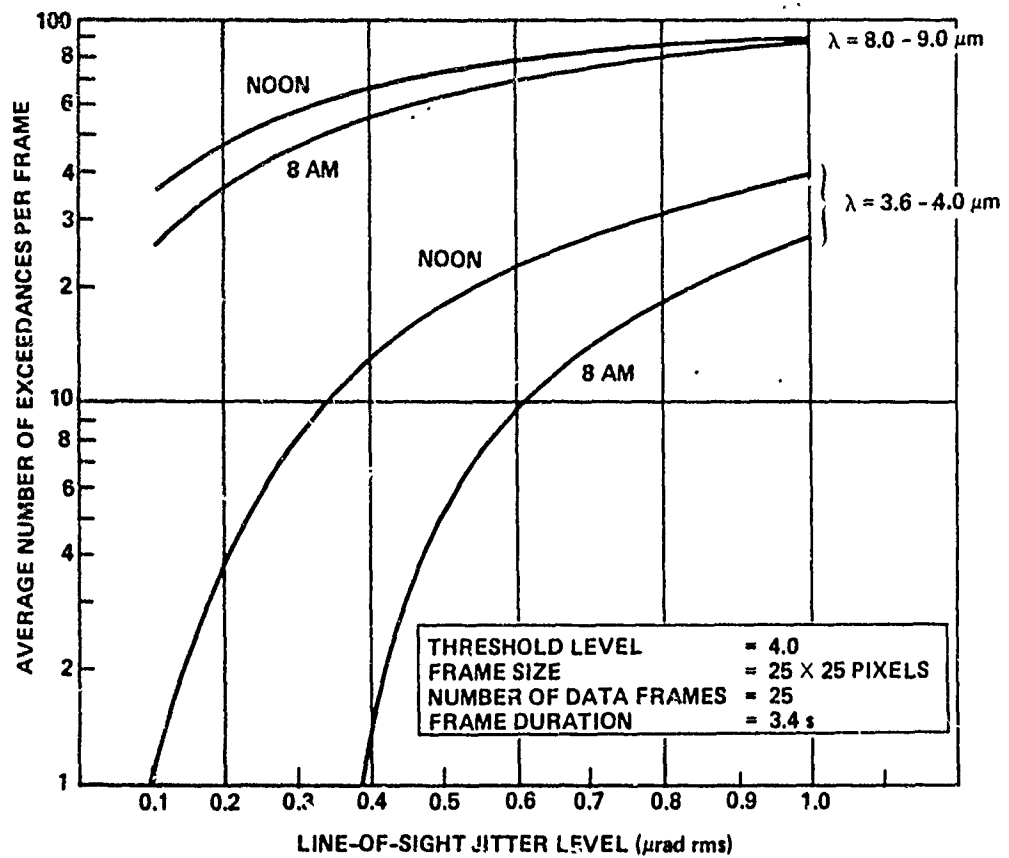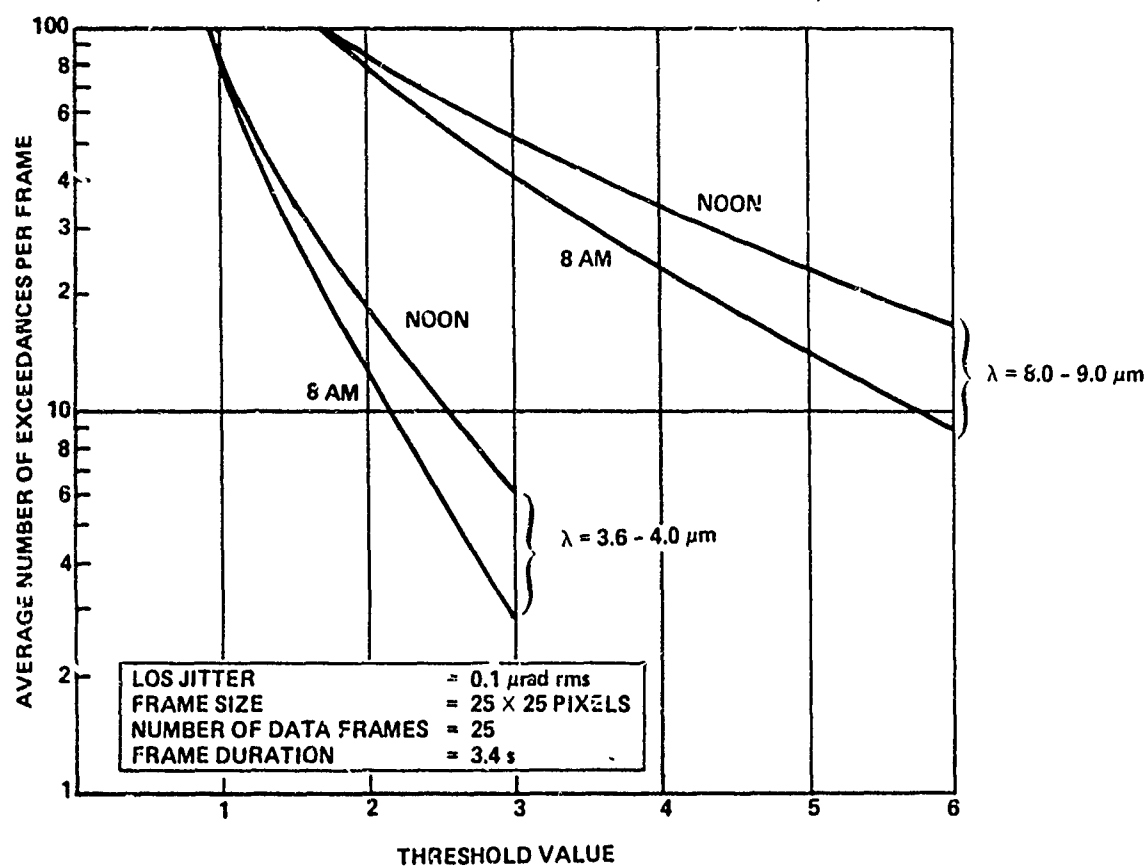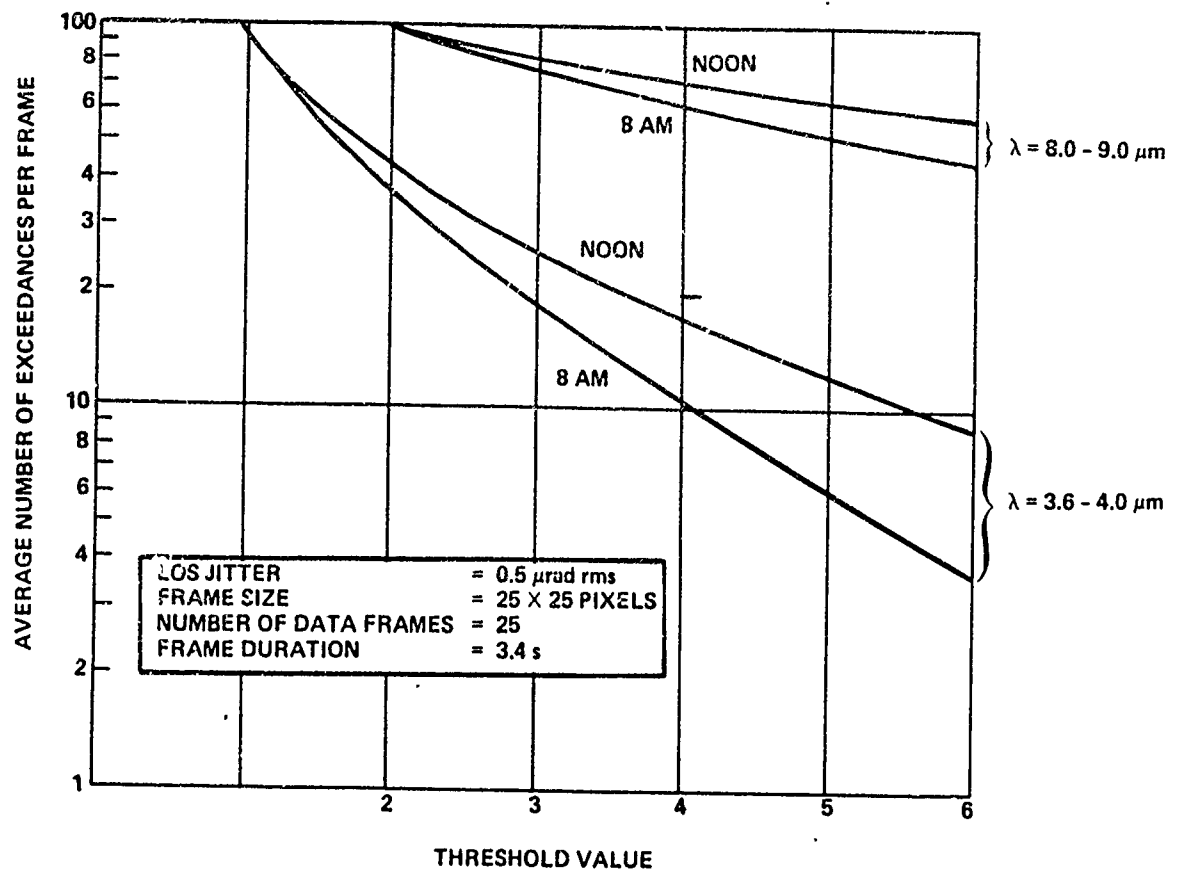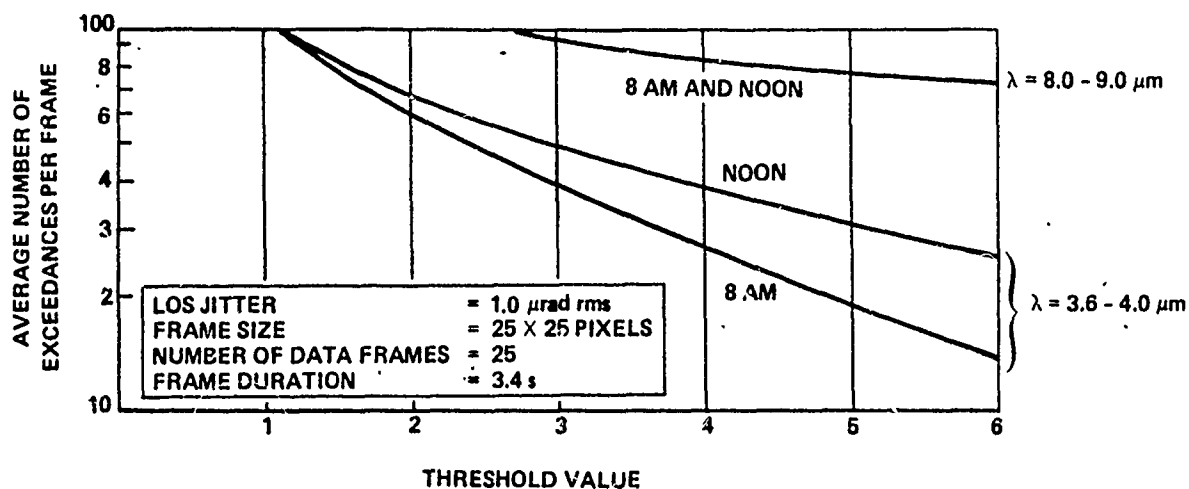Figure 2-7. Average clutter leakage as a function of threshold level for the GENESSIS Santa Cruz scene, with local time of day and spectral band as parameters. (LOS Jitter = 1.0 μrad RMS)

threshold values, as can be seen by comparing Figures 2-5 and 2-6. In addition, there is a compression within each spectral band of the exceedance curves corresponding to noon and to 8 AM. In Figure 2-7, an LOS jitter level of 1.0 μrad RMS (ten times the value used in Figure 2-5) results in the coalescing of these two curves for the LWIR band.

A subject of great interest in the study of signal processor performance and scene/sensor interaction is a determination of the conditions under which false target tracks arise. Figure 2-8 summarizes graphically the false tracks which resulted during the course of the present study. Separate numbers, i.e., "1" versus "2", are used to designate the relative position of distinct tracks within the overall 25 × 25 pixel field-of-view. Consistent with the data presented in Figures 2-4 through 2-7, false tracks were found at low threshold levels where the average number of exceedances is very high. Under these conditions the likelihood of a time sequence of individual exceedances occurring in such a fashion as to satisfy the signal processor track formation and acquisition criteria is considerably increased.

2.4   Conclusions

The focal plane and signal processor simulation enhancements are complete, and the platform simulation enhancements are in process and proceeding satisfactorily. Phase I of the Generic Scene Simulation (GENESSIS) activity is complete and operational at CSDL. The last phase of this activity is currently in process under subcontract to CSDL at Photon Research Associates. The Draper Integrated Simulations thus represent a highly sophisticated tool for end-to-end performance trade-offs of a variety of space-based systems, and especially staring mosaic IR surveillance systems.

LOS-induced clutter leakage through the signal processor has been simulated as a function of spectral interval and scene time-of-day for a generic staring mosaic IR surveillance system. The functional dependence of the scene/sensor interaction is complex and has been described quantitatively by a series of curves showing average number of threshold exceedances per frame both as a function of LOS jitter for a particular threshold and as a function of threshold for particular LOS jitter values. Qualitatively it is clear that increased LOS jitter yields increased clutter leakage in all cases considered. Clutter leakage in the short-wave infrared (SWIR) band of 3.6-4.0 μm is significantly less than in the long-wave infrared (LWIR) band of 8.0-9.0 μm. For either SWIR or LWIR, clutter leakage at noon (local time) is greater than early morning. For a fixed threshold value, increased LOS jitter drives early morning clutter levels toward noon clutter levels in both the SWIR and the LWIR bands. And, finally, low threshold values in the presence of LOS jitter can result in the generation of false acquired tracks.
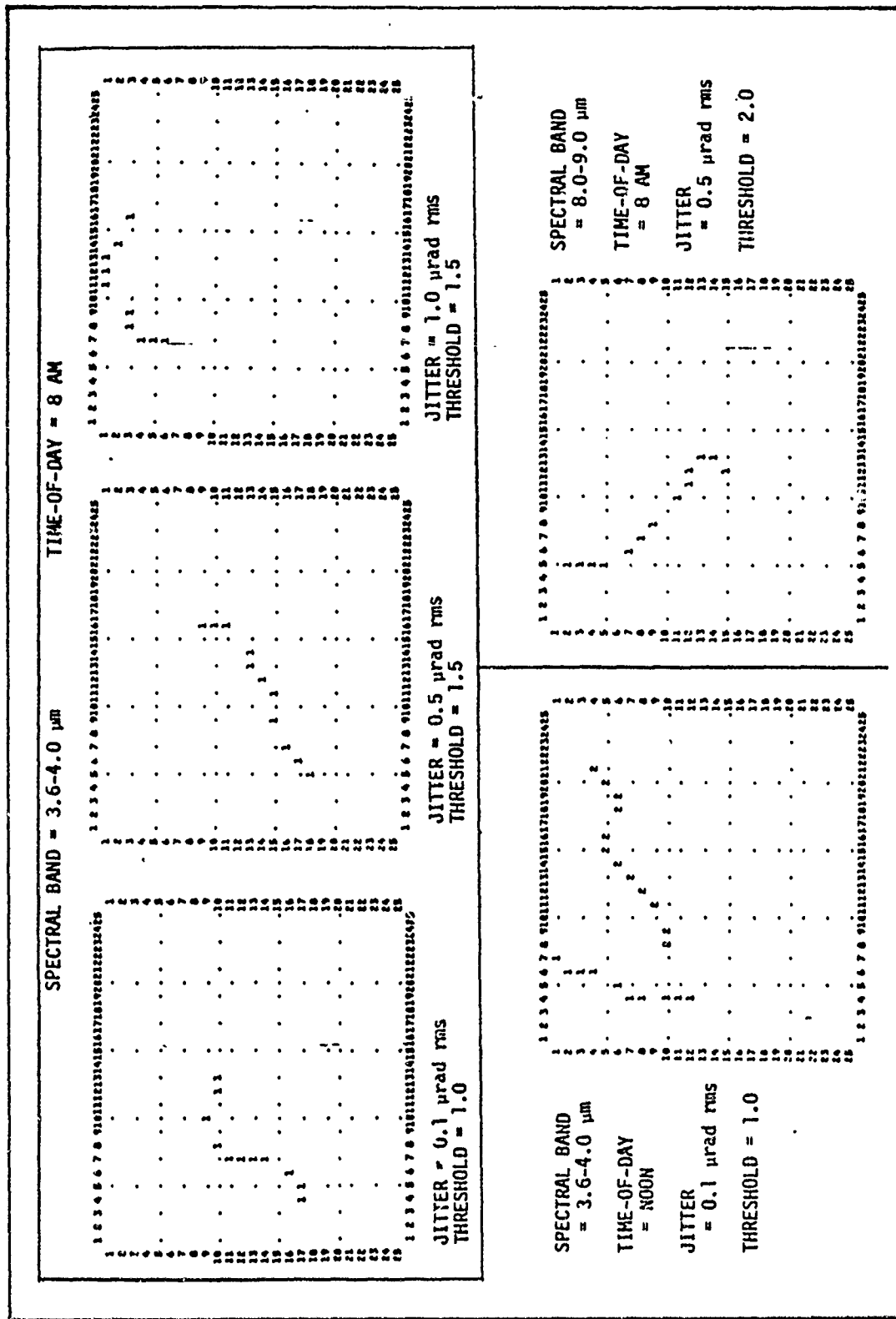
Figure 2-8. False tracks induced by LOS jitter in the GENESSIS Santa Cruz scene.

SECTION 3

HALO OPTICS
DECONVOLUTION TEST

3.1   Introduction

HALO is a multi-mirror large optical imaging system with a wide field
of view. To maintain alignment as well as image quality, the mirrors are
actively controlled with actuators. The term "deconvolution" implies a
sensing and control scheme by which a deformed HALO optical system is cor-
rected in near real time. In one of the techniques worked on by the Itek
Corporation, the wavefront errors of the deformed system are measured with a
wavefront sensor for several object points near the edge of the field-of-
view of the system. The wavefront sensor is placed around the focal plane.
The wavefront errors are decomposed into mirror figure errors and actuator
displacements are generated to correct them with a deconvolution algorithm.
This report describes a limited blind test that CSDL prepared for Itek to
test and validate this algorithm. We conclude that the algorithm success-
fully determined the actuator displacements from the wavefront errors.

3.2   Optical System for Deconvolution Test

For a hardware demonstration of their deconvolution algorithm, Itek
has been planning to use an optical imaging system consisting of three
active flat mirrors and a pair of lens doublets mounted back-to-back in a
1:1 magnification. A schematic of this system is shown in Figure 3-1.

The lenses are the imaging elements of the system, and the mirrors
are the deformable elements. Aberrations are introduced into the system by
deforming the mirrors. The active mirrors, thus simulate the deformable
aspects of a HALO system. The footprints on the mirrors of rays from a
given point object are similar to those on the S-HALO or WALRUS mirrors. A
perspective view of the optical system is given in Figure 3-2. It shows the
coordinate system chosen to designate the actuator and ray distributions.

3.3   Actuator Distribution and Influence Function

Each of the three mirrors has 37 actuators distributed on an equi-
lateral triangular lattice as shown in Figure 3-3. In consultation with
Itek, the influence function of the actuators was chosen to be similar to
the one for active mirrors developed for the compensated imaging program.
This influence function is given by

$$f(r) = \left[1 - 1.2(r/d)^2\right]^2 \quad , \quad r \leq d/\sqrt{1.2} \quad ,$$

$$= 0 \quad , \quad r > d/\sqrt{1.2} \quad ,$$

where
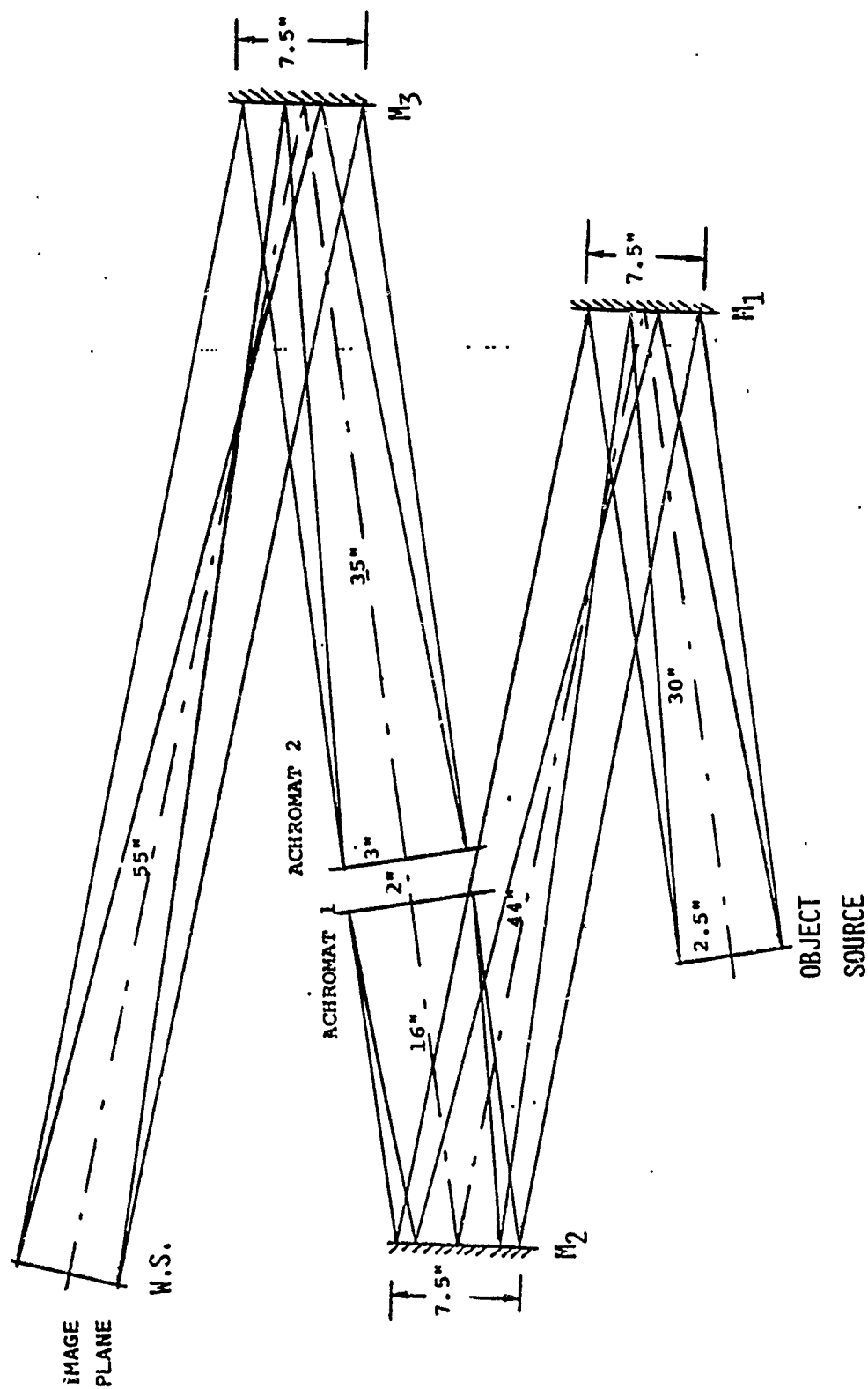
Figure 3-1. Schematic of the optical system used for the deconvolution test. The lenses are the imaging elements and the three active mirrors simulate the deformable aspects of a HALO system.
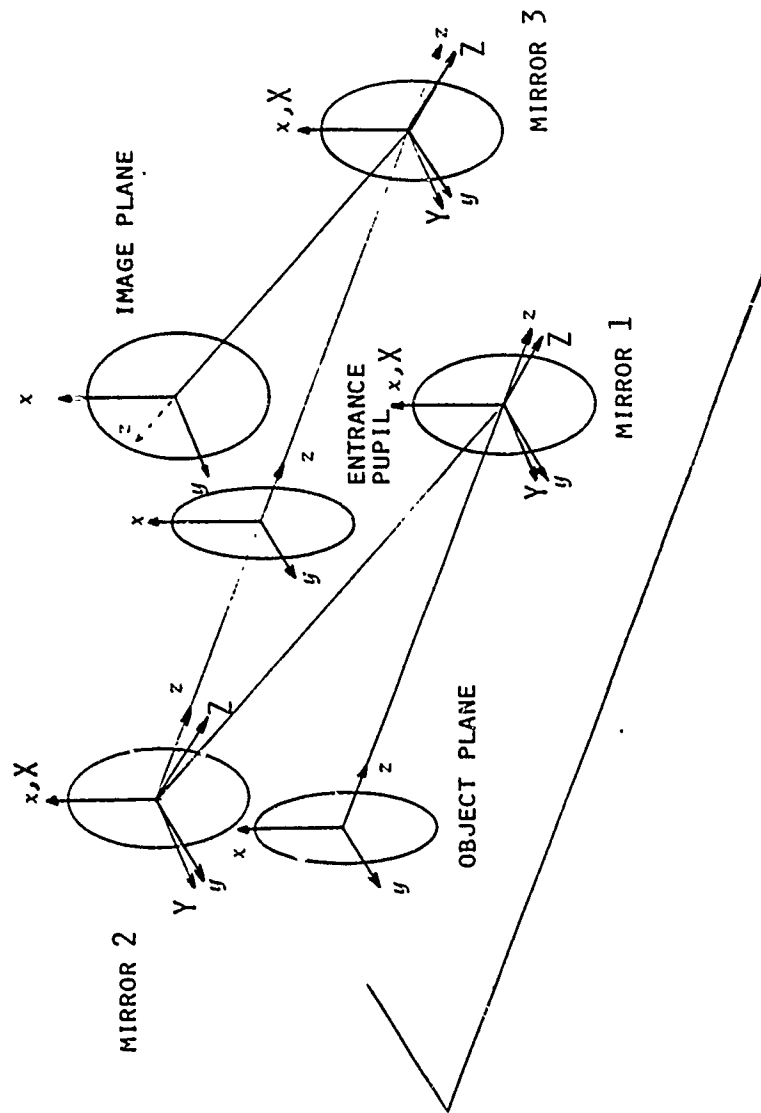
Figure 3-2. Perspective view of the optical system illustrating the coordinate system used for actuator and ray distributions. (X,Y,Z) is the coordinate system used to describe mirror deformations. (x,y,z) is the coordinate system used for ray tracing.
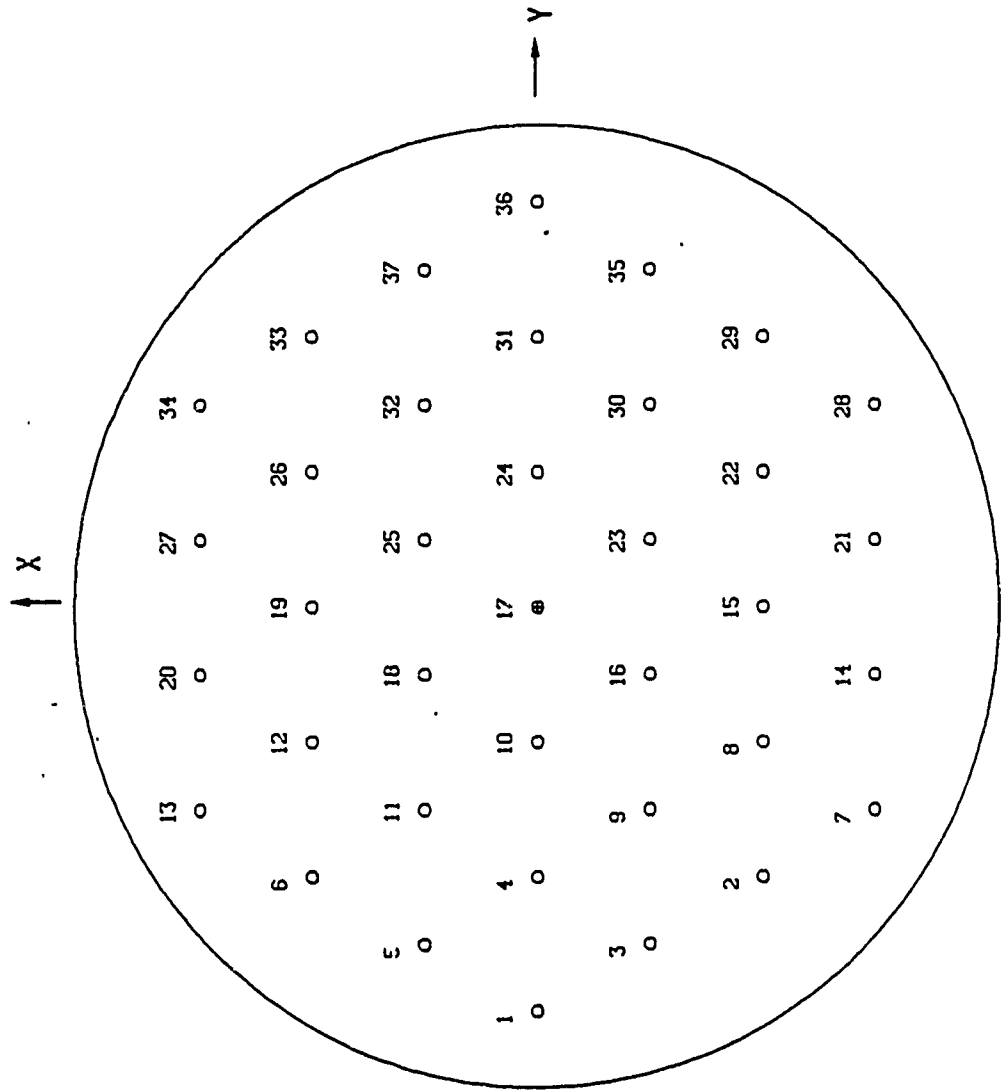
Figure 3-3. Actuator distribution on mirrors.

r = distance from the actuator,

d = actuator spacing.

The variation of f(r) with r is shown in Figure 3-4. It is noted that the influence function is radially symmetrical about the actuator position. Moreover, one actuator does not produce any influence on another. The factor of 1.2 was chosen to minimize the effect of quilting when all actuators are displaced by the same amount. With a 1.2 factor, quilting is at most 8%. When an actuator is displaced by an amount h, the deformation produced in the mirror is given by hf(r). In our problem d $\simeq$ 3cm.

3.4   Mirror Deformations

The deformations of the mirrors used in the deconvolution test are given in Figure 3-5. The numbers in this figure give the actuator displacements in units of $\lambda/100$. Mirror M_1 was deformed according to cryogenic deformations of an Itek HALO mirror. Mirror M_2 has deformations described by Zernike polynomials representing coma and astigmatism. Mirror M_3 was given a rigid-body displacement along its normal. The mean, peak-to-peak, and standard deviation of the actuator displacements are indicated in the figure for each mirror.

## 3.5   Selection of Point Objects

Nine point objects were selected for ray tracing and determining the system wavefront errors. Eight of these are uniformly distributed around the edge of the field-of-view of the system (1.5° from the axis), and one is placed on the system axis as indicated in Figure 3-6. The on-axis point object was used only for the sake of completeness to include the deformations of the central portion of mirror M_1. The wavefront sensors placed around the focal plane cannot sense the effect of these deformations.   In practice, the central portion of M_1 will, for example, be corrected by CSDL's image sharpening approach.[1,2]

3.6   Mirror Footprints

Figure 3-7 shows the footprint on the mirrors of the image forming rays from point objects 1 and 2. We note that, as in a HALO optical system, the footprints of rays from point objects such as 2, near the edge of the field of view, on mirrors M_1 and M_2 cover the mirror portions used in imaging. However, their footprint on mirror M_1 is not only small compared to the mirror size, but also it is off the mirror center. Accordingly, the footprints of the rays from the 8 off-axis point objects cover the outer portion of the mirror M_1 but not its central portion.

The image of the on-axis point object is formed at the center of the focal plane. The central portion of mirror M_1 can be corrected by the image sharpening technique using the focal plane data.
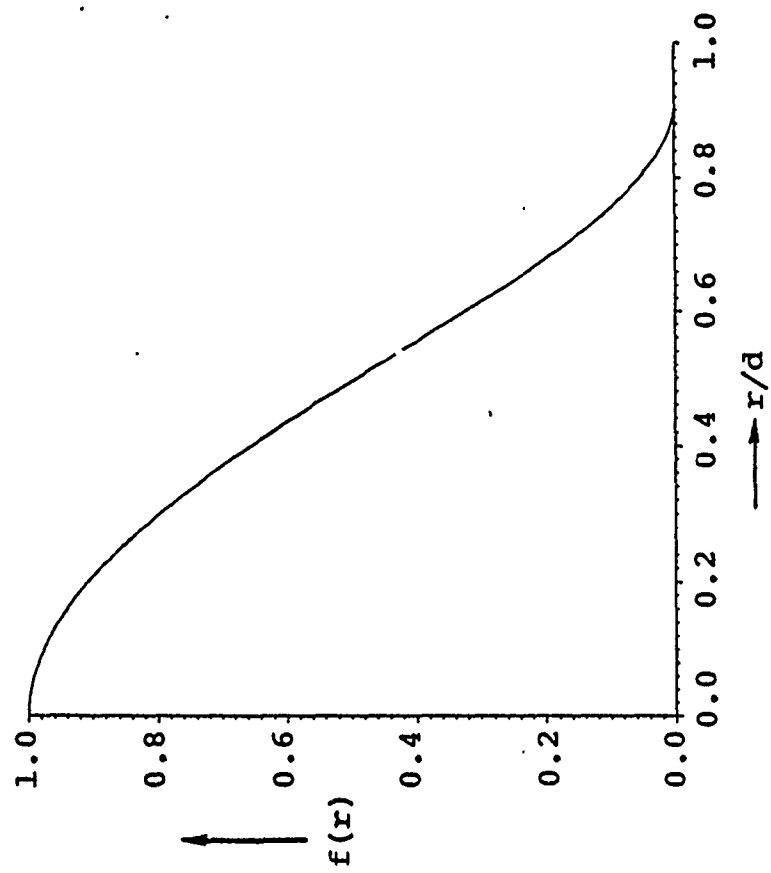
Figure 3-4. Actuator influence function.

24
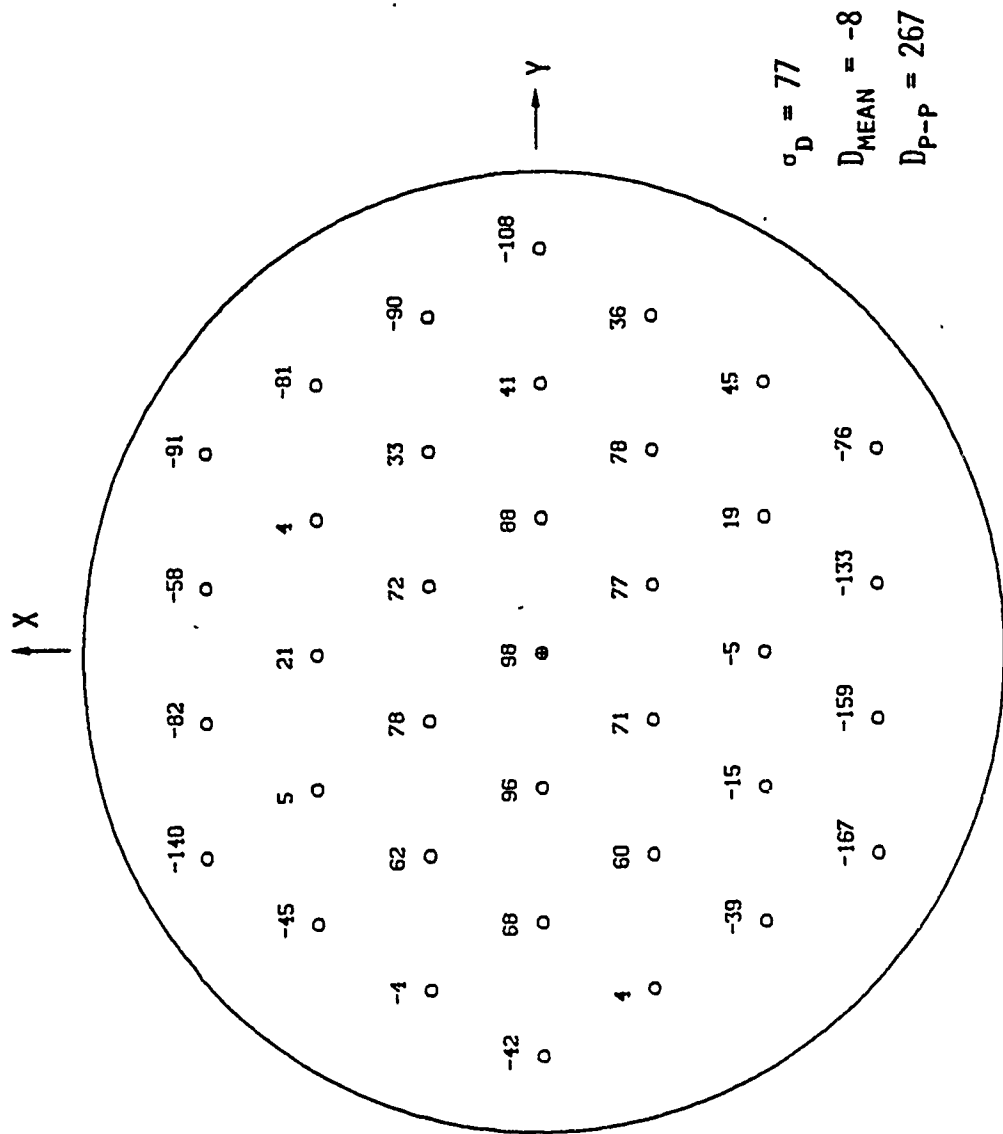
Figure 3-5. Actuator displacements in units of $\lambda/100'$ indicating deformations.
a. Mirror 1. $\sigma_D = 77$, $D_{mean} = -8$, $D_{p-p} = 267$.
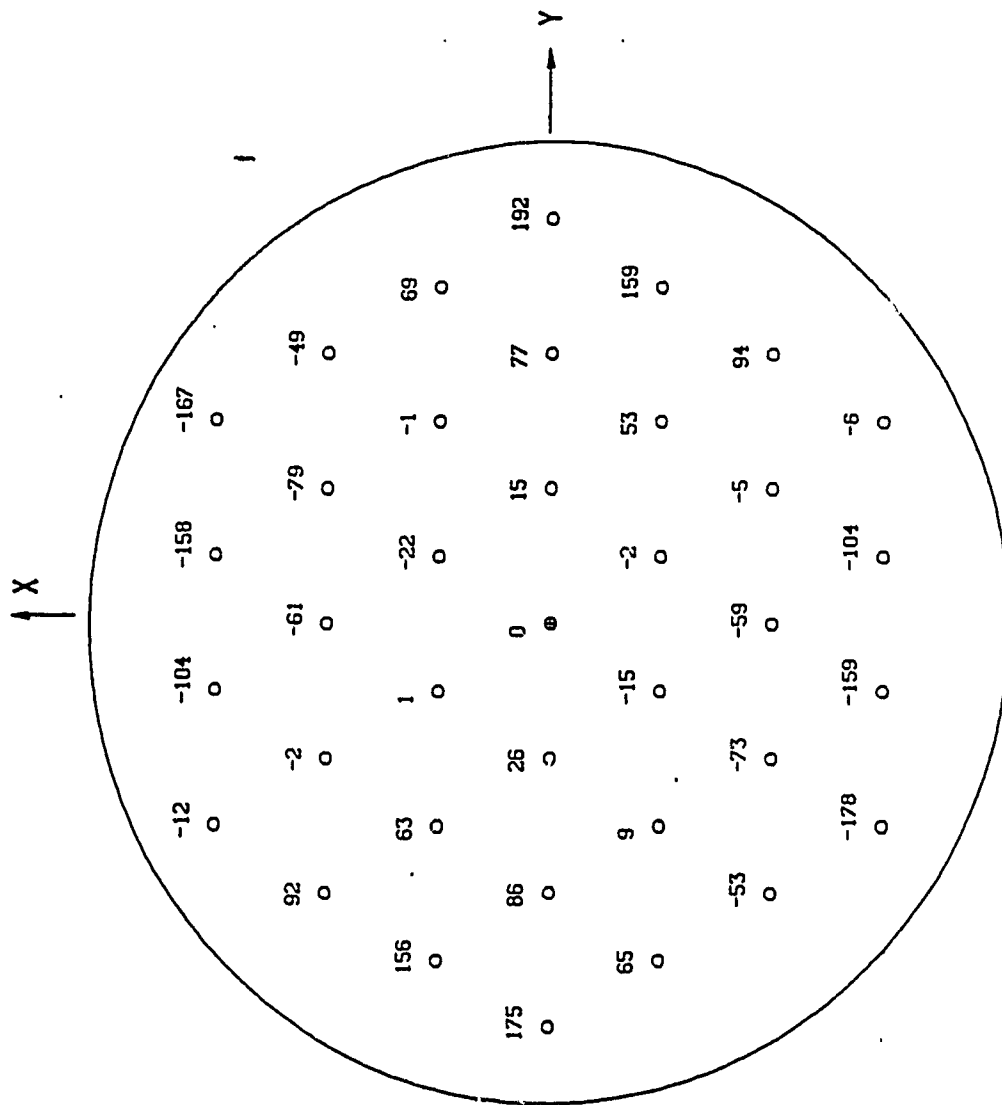
Figure 3-5b. Mirror 2. $\sigma_D = 94$, $D_{mean} = 0$, $D_{p-p} = 371$.
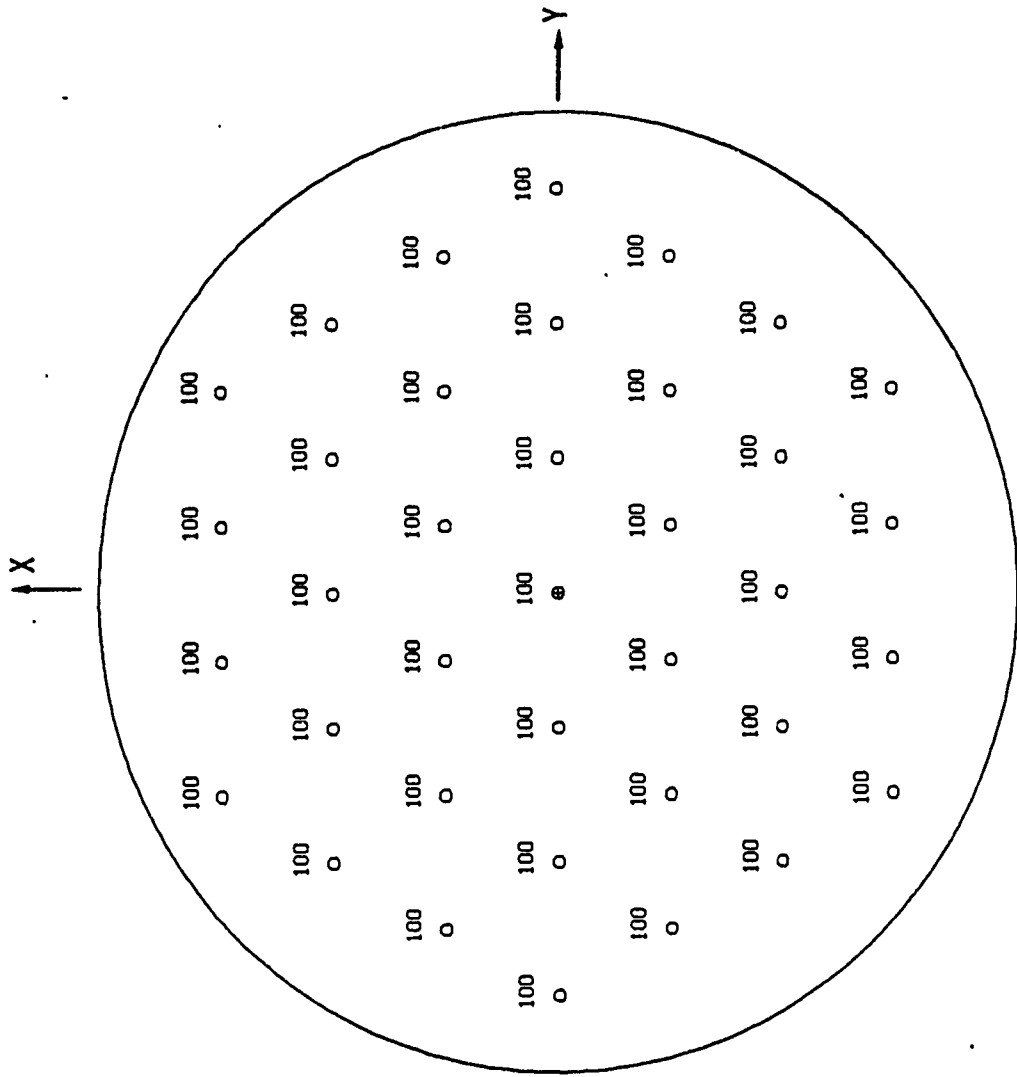
Figure 3-5c. Mirror 3. $\sigma_D = 100$, $D_{mean} = 100$, $D_{p-p} = 100$.

27
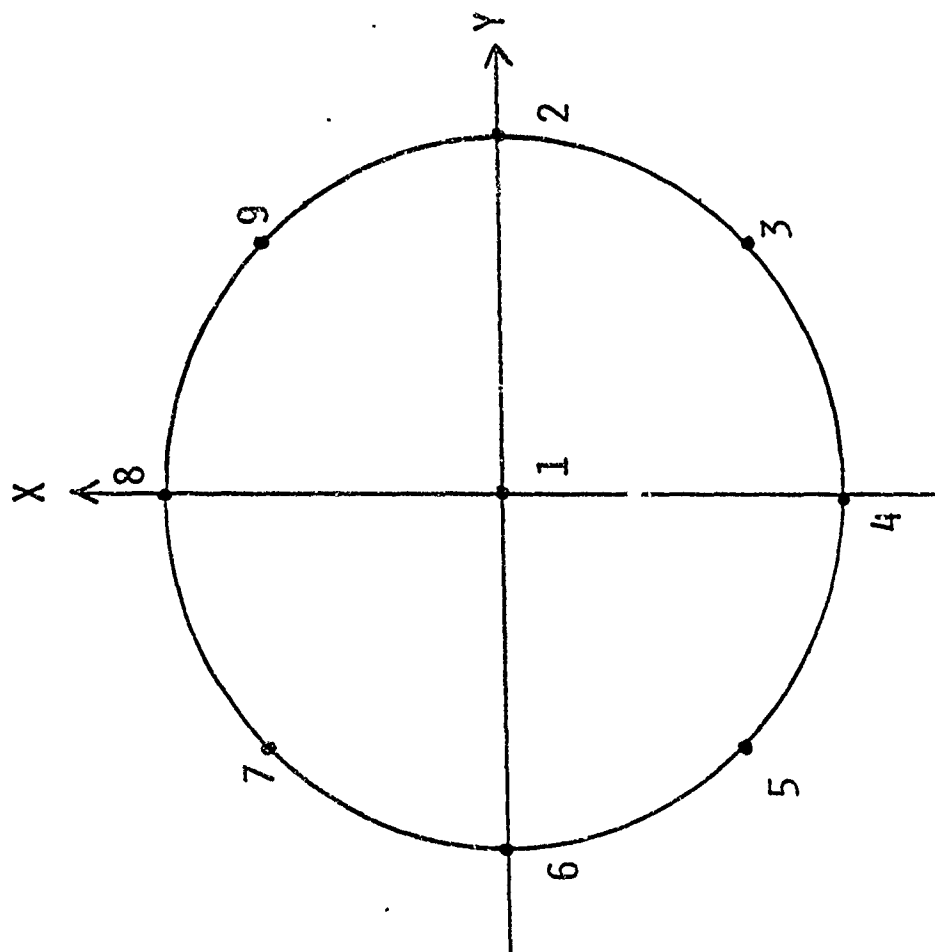
Figure 3-6. Distribution of point objects used for determining system wavefront errors.
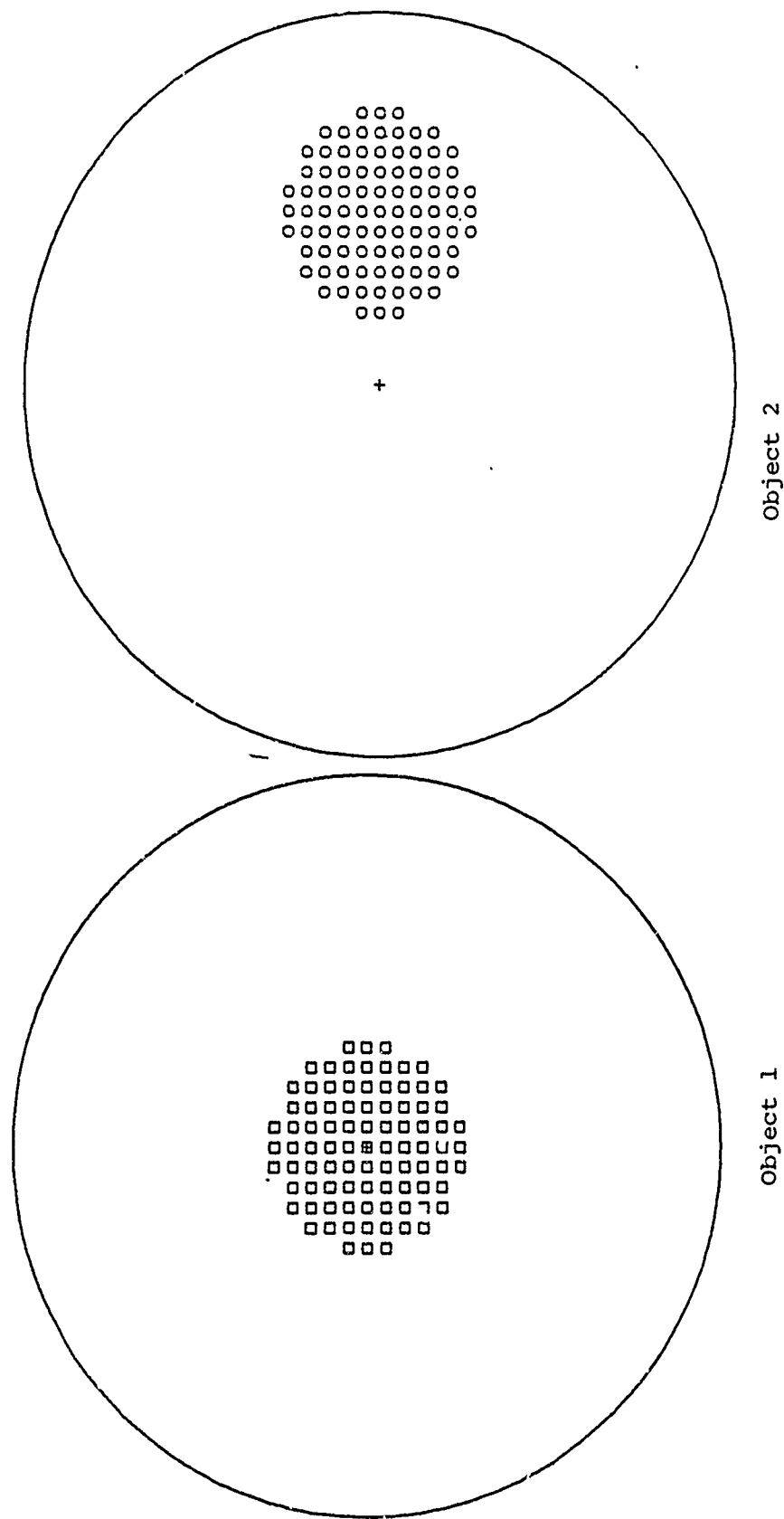
Object 1   Object 2

Figure 3-7. Footprints of image forming rays on mirrors.
              a. Mirror 1.
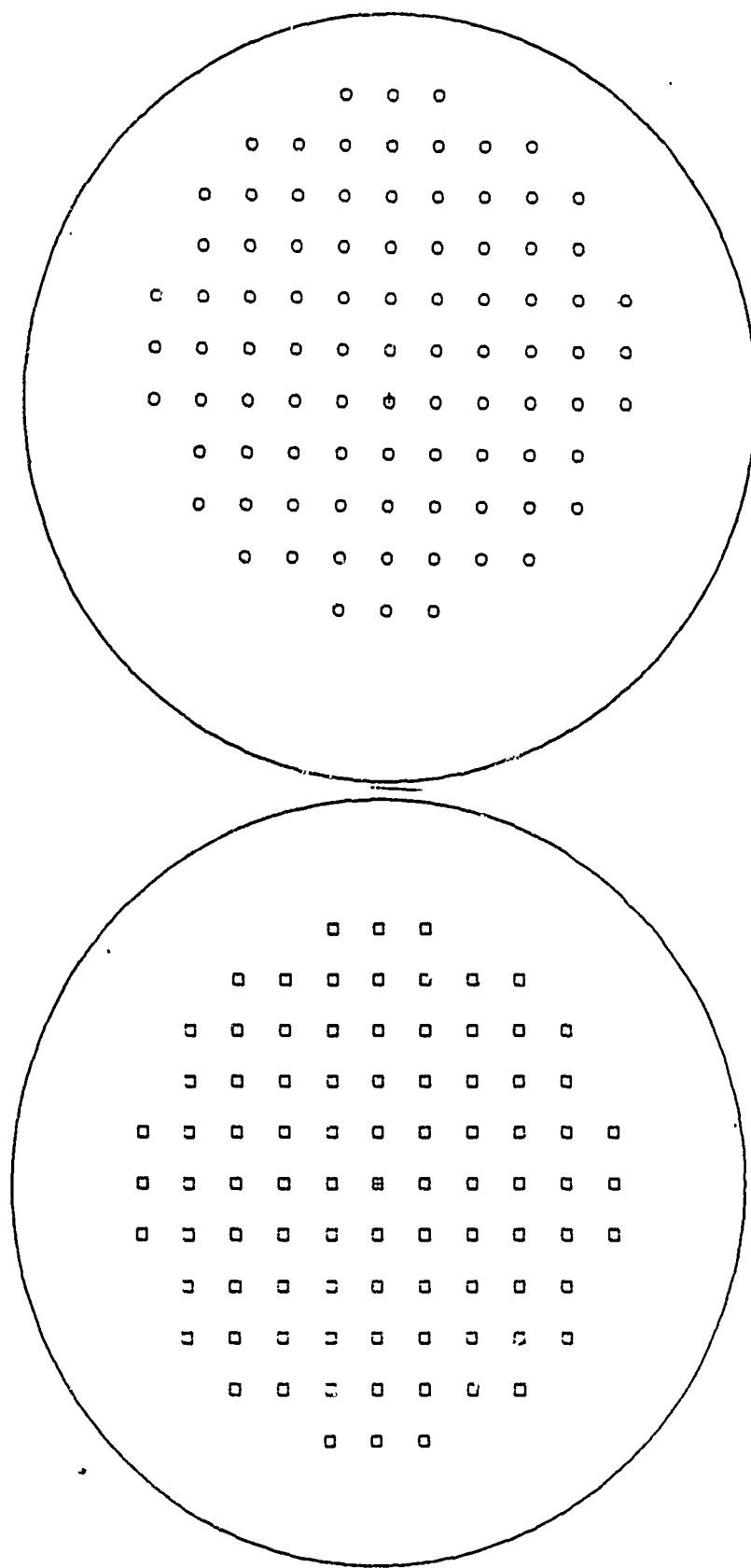
Object 2

Object 1

Figure 3-7b. Mirror 2.

30
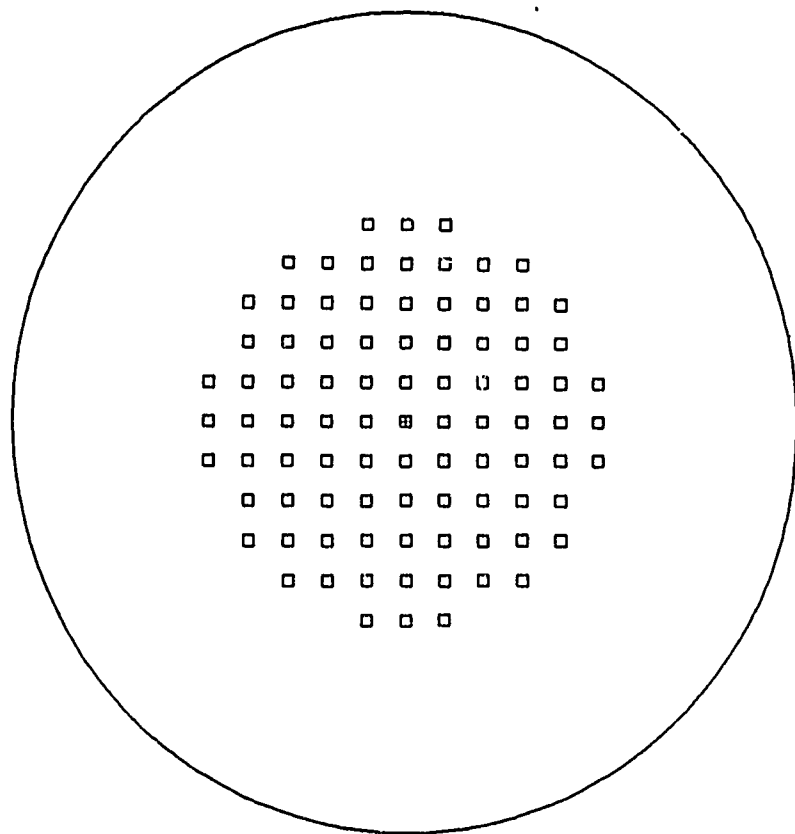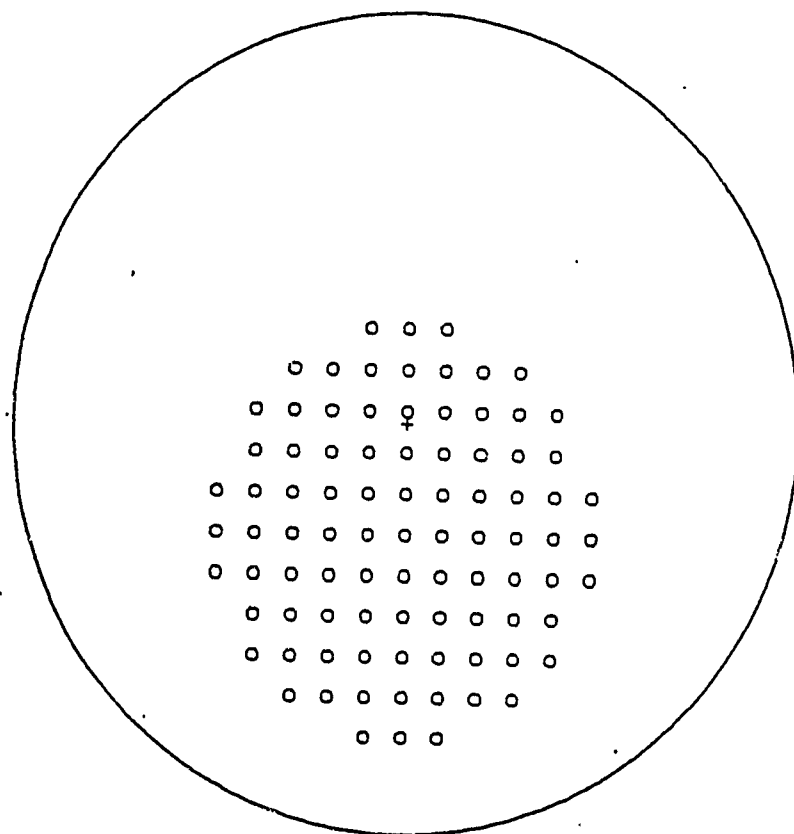
Object 1   Object 2

Figure 3-7c.   Mirror 3.

31

3.7 Wavefront Errors

When the optical system deforms, the wavefront error introduced at a certain point on the wavefront is given by the change in the path length of a ray passing through that point. The change in the path length of a ray from a given point object in terms of the mirror deformations is given according to[3]

$$\Delta W_i = 2 \sum_{m=1}^{3} \hat{n}_{im} \cdot \vec{\delta r}_{im} \cos \theta_{im},$$

where

$\hat{n}_{im}$ = unit vector along the normal to the surface of undeformed mirror m at the point of incidence of the ray i,

$\vec{\delta r}_{im}$ = displacement of the point of incidence of ray i on mirror m,

θ_{im} = angle of incidence of ray i on the undeformed mirror m.

Since we are dealing with flat mirrors, n_{im} for a given mirror is independent of i.

Figure 3-8 shows the distribution of 89 rays in the pupil used for determining the wavefront errors. The wavefront errors corresponding to point objects 1 and 2 when the optical system is deformed according to mirror deformations of Figure 3-5 are given in Figure 3-9. These wavefront errors include $\lambda/20$ random error to simulate the noise of a wavefront sensor. We provided Itek with noisy wavefront errors at 89 points for each of the nine point objects.

3.8 Test Results

3.8.1 Mirror Deformations

From the wavefront error data for the nine point objects we provided to Itek, they determined the actuator corrections (displacements) required to correct the figure of the mirrors to reduce the wavefront errors. The actuator corrections determined by their deconvolution algorithm are given in Figure 3-10. The residual errors obtained by subtracting these corrections from the errors given in Figure 3-5 are also shown in Figure 3-10. The mean and the standard deviation of the residual displacements are listed in the figure for each of the three mirrors. We note that the residual errors are quite small except for the corner actuators. The region of mirrors where corner actuators are located is not used for imaging. Hence, the effect of these actuators on the mirror figure is not observed by the wavefront sensor.
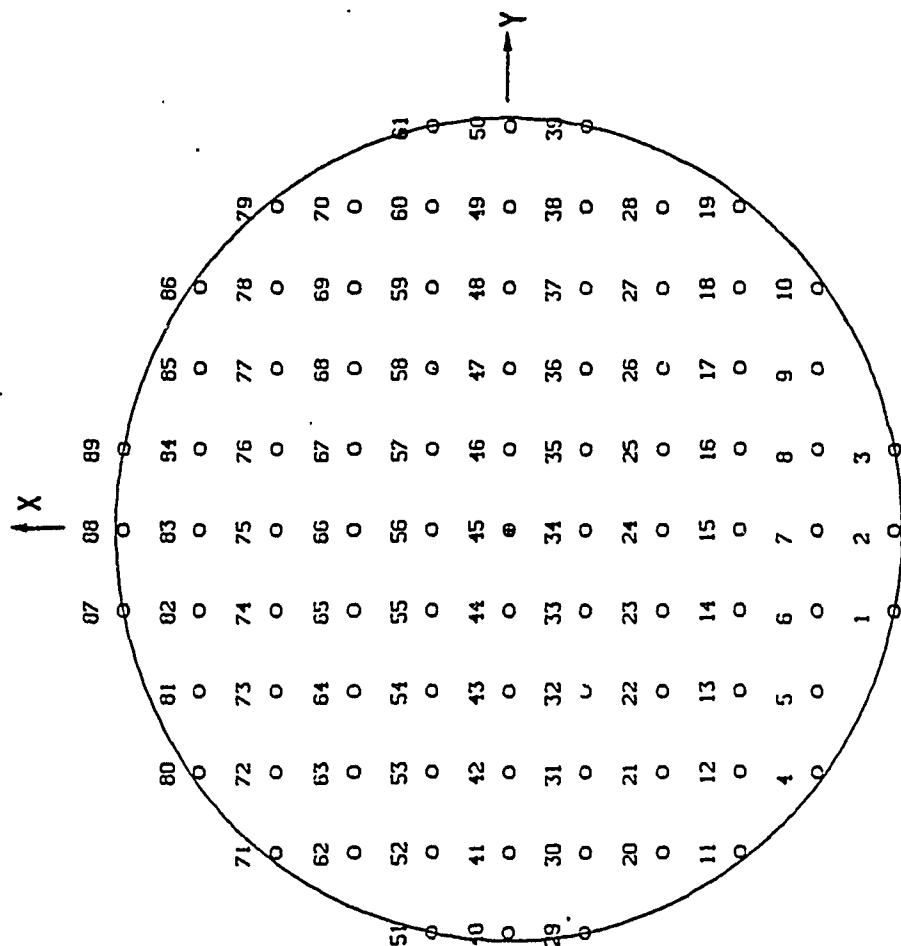
Figure 3-8. Distribution of rays in the pupil.
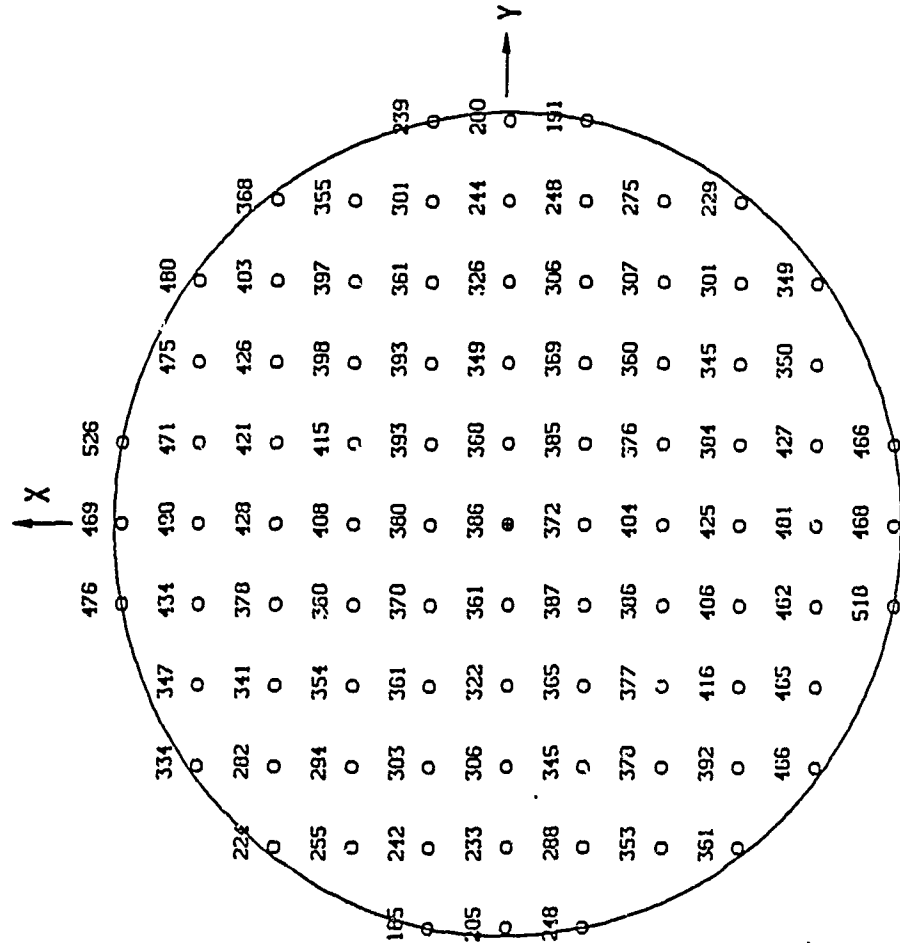
Figure 3-9. Wavefront errors with noise in units of $\lambda/100$
a. Object 1. $\sigma_W = 78$, $W_{mean} = 362$, $W_{p-p} = 200$.
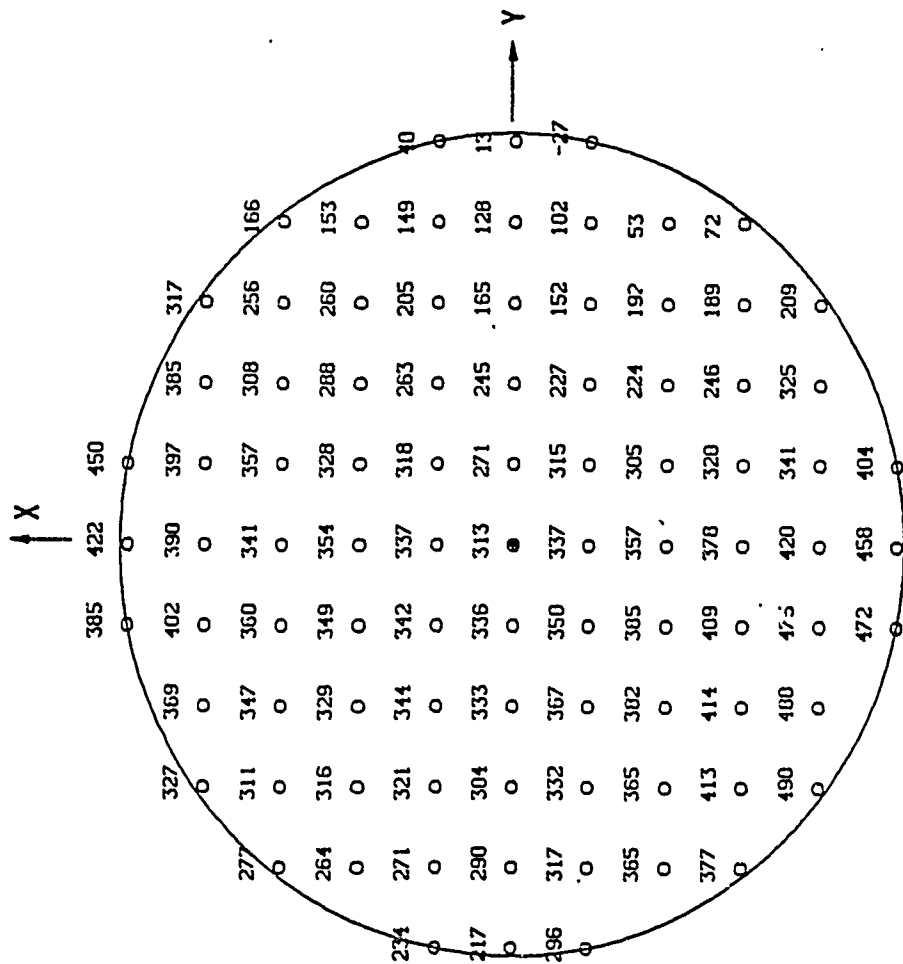
Figure 3-9b. Object 2. $\sigma_W = 106$, $W_{mean} = 303$, $W_{p-p} = 237$.

Residual Errors

$\sigma_D = 39$, $D_{mean} = -13$

Corrections

$\sigma_D = 66$, $D_{mean} = 66$

Figure 3-10. Actuator corrections and residual errors (in units of $\lambda/100$).
a. Mirror 1.

Residual Errors

$\sigma_D = 5$, $D_{mean} = 1$

Corrections

$\sigma_D = 95$, $D_{mean} = -1$

Figure 3-10b. Mirror 2.

37

Residual Errors

$\sigma_D = 16$, $D_{mean} = 9$

Corrections

$\sigma_D = 16$, $D_{mean} = 91$

Figure 3-10c. Mirror 3.

38
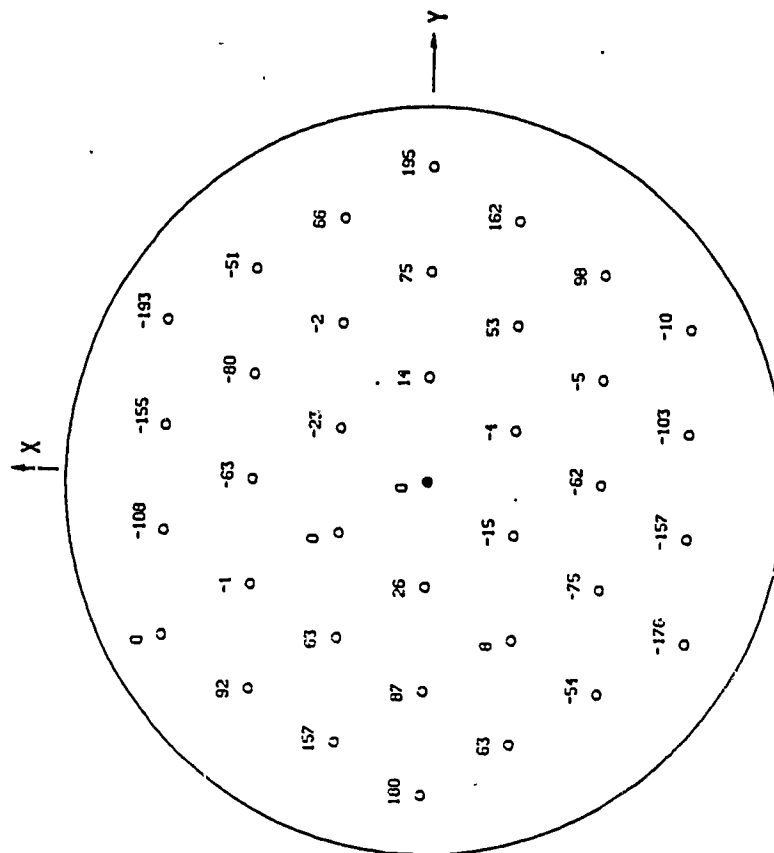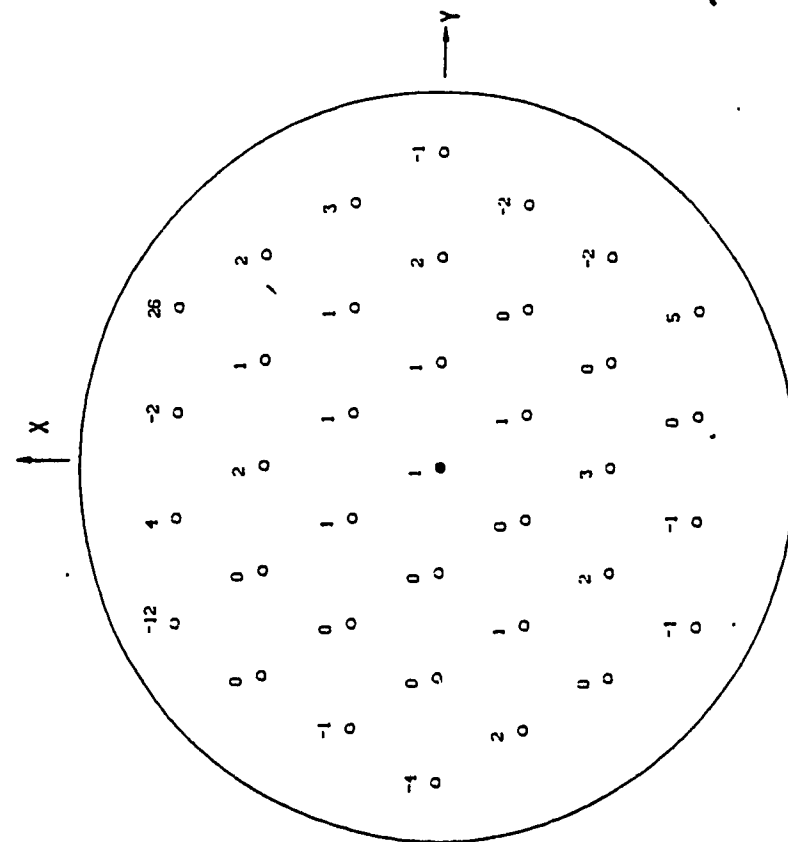
3.8.2 Wavefront Errors

The wavefront errors of the corrected system were determined by tracing 89 rays as in the case of the deformed system. These errors were quite small ($\sigma_w < \lambda/40$) indicating an excellent correction. Random noise of $\lambda/20$ was added to these errors to simulate the wavefront errors that a wavefront sensor would measure. The noisy residual wavefront errors for point objects 1 and 2 are shown in Figure 3-11. The mean, peak-to-peak, and standard deviation of the wavefront errors are also given. It is evident from the standard deviation that most of the error is indeed due to the wavefront sensor.

3.8.3 Point-Spread Functions

The aberrated and the corrected point-spread functions for point objects 1 and 2 are shown in Figures 3-12 and 3-13, respectively. The standard deviation of the aberration, the Strehl ratio (aberrated irradiance at the center relative to its unaberrated value) and peak irradiance are also given in the figures. For example, for point object 1, the deformed system gives a Strehl ratio of only 0.025. The light is spread over a region $31\lambda F$ wide compared with approximately $2\lambda F$ for the corrected (or aberration-free) system. With a correction determined by Itek deconvolution algorithm, a Strehl ratio of approximately 0.95 is obtained. The corrected Strehl ratios in Figures 3-12 and 3-13 are slightly lower because of the wavefront sensor noise.

3.9   Discussion, Conclusions, and Recommendations

An optical system using three flat mirrors as deformable elements has been used for testing the deconvolution algorithm developed by Itek. Each mirror has 37 actuators, and 89 rays have been used to determine wavefront errors of a deformed system. CSDL provided Itek with a known-deformation test and a blind test. The known-deformation test was prepared so that CSDL and Itek softwares could be tested for compatibility. On the blind test, two of the 9 wavefronts that Itek was given are shown in Figure 3-9.

Itek's deconvolution algorithm determined the actuator displacements on each mirror and these were subtracted from the input displacements given in Figure 3-5. The corrected system was ray-traced to determine its imaging quality. It gave a Strehl ratio of approximately 0.9 indicating an excellent correction.

We conclude that Itek's deconvolution algorithm successfully determined the actuator displacements from the wavefront errors. The residual wavefront errors were negligibly small and below the wavefront sensor noise.

We recommend that one more blind test be prepared for Itek's deconvolution algorithm to include more realism. Some of the desirable features of this test are listed below.

39

Object 2

$\sigma_W = 6$, $W_{mean} = 12$, $W_{p-p} = 28$

Object 1

$\sigma_W = 5$, $W_{mean} = 8$, $W_{p-p} = 22$
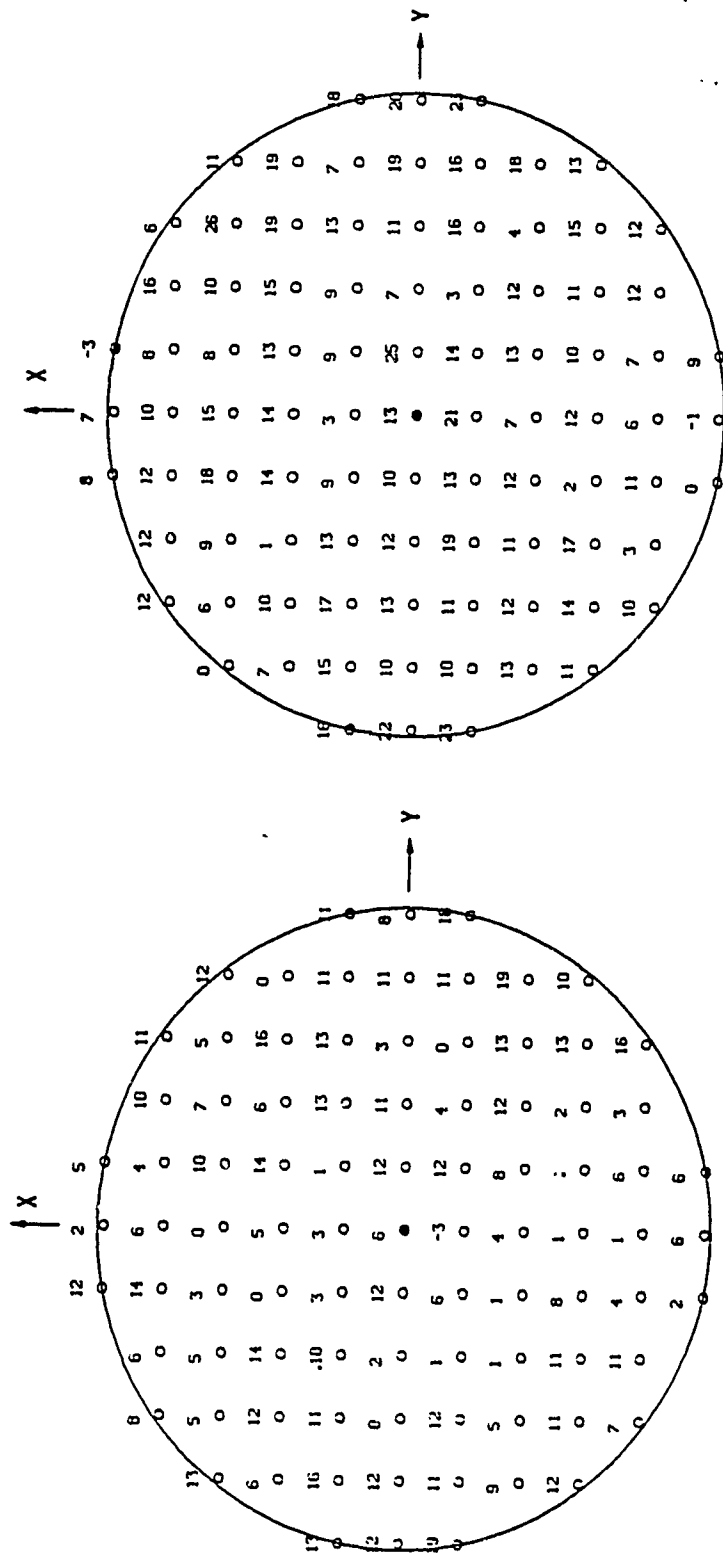
Figure 3-11. Residual wavefront errors (in units of $\lambda/100$).

40
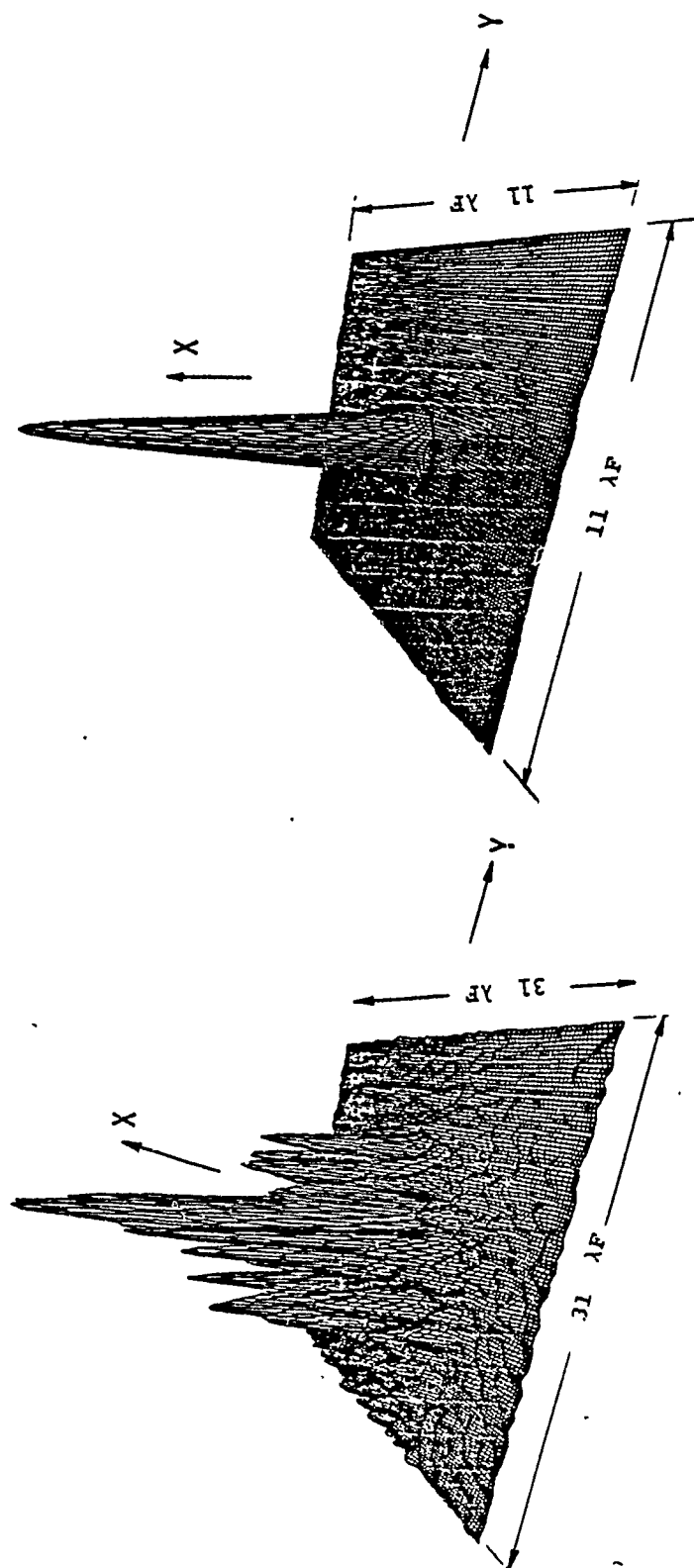
Aberrated

Corrected

$\sigma_W = 0.78\lambda$, Strehl = 0.025, Peak = 0.047 $\sigma_W = 0.051\lambda$, Strehl = 0.902, Peak = 0.092

Figure 3-12. Point-spread function for point object 1. The quantities λ and F are the optical wavelength and system focal ratio (f/#).

41

Corrected
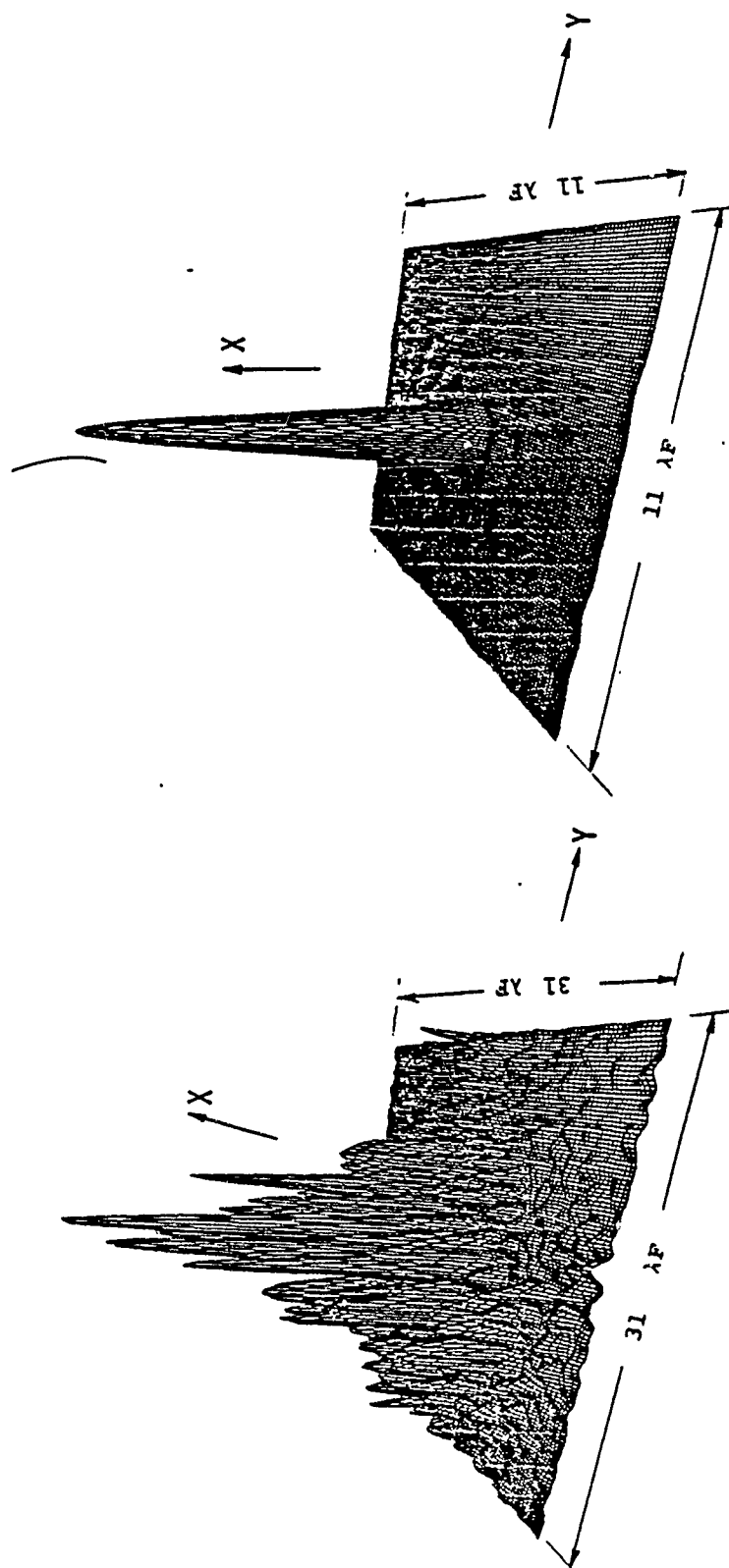
Aberrated

$\sigma_W = 0.058$, Strehl = 0.896, Peak = 0.896

$\sigma_W = 1.06$, Strehl = 0.0038, Peak = 0.064

Figure 3-13. Point-spread function for point object 2.

42

1. Mirror deformations will not be produced by the actuators used for correction, because, in practice, a mirror is not deformed by the movement of actuators.

2. Some static aberrations will be added to the optical system to simulate a nondiffraction-limited undeformed system.

3. The on-axis wavefront error data may not be provided, since the wavefront sensor placed around the HALO focal plane can not sense it.

4. The actuator influence functions used for mirror figure correction will be slightly different from those used by Itek in their algorithm, to simulate errors in the knowledge of influence function.

5. The influence function for edge actuators may be different from that for interior actuators.

6. A segmented mirror will be used.

7. The mirror size will be approximately the same as the illuminated region.

References

1. V.N. Mahajan, J. Govignon, and R.J. Morgan, "Adaptive Optics Without Wavefront Sensors," Proc. SPIE 228 63-69 (1980).

2. V.N. Mahajan, "ACOSS Eleven Second Semiannual Technical Report, Volume 1," CSDL-R-1583, August 1982.

3. V.N. Mahajan and J. Govignon, "Computer Simulation of a Large Adaptive Optical System," Proc. SPIE 172 439-451 (1979).

addresses

number
of copies

Richard Carman
RADC/OCSE   5

RADC/TSTD
GRIFFISS AFB NY 13441   1

RADC/DAP
GRIFFISS AFB NY 13441   2

ADMINISTRATOR
DEF TECH INF CTR   12
ATTN: DTIC-DDA
CAMERON STA BG 5
ALEXANDRIA VA 22314

Charles Stark Draper Lab
555 Technology Square   5
Cambridge, MA 02139

Charles Stark Draper Lab
Attn: Dr. Keto Soosaar   1
555 Technology Square
M.S. -95
Cambridge, MA 02139

NASA Headquarters
ATTN: Mr. J. B. Dahlgren   1
Code RTH-6
Washington, DC 20546

Charles Stark Draper Lab
Attn: Mr. R. Strunce   1
555 Technology Square
M.S. -60
Cambridge, MA 02139

Charles Stark Draper Lab
Attn: Dr. Daniel R. Hegg   1
555 Technology Square
M.S. -60
Cambridge, MA 02139

```
ARPA/STO                                                    1
Attn: Lt Col A. Herzberg
1400 Wilson Blvd
Arlington, VA 22209


ARPA/STO                                                    1
Attn: Maj E. Dietz
1400 Wilson Blvd
Arlington, VA 22209


Riverside Research Institute                               2
Attn. Mr. A. DeVilliers
1701 N. Ft. Myer Drive, Suite 711
Arlington, VA 22209


Riverside Research                                         1
Attn: HALO Library, Mr. Bob Passut
1701 N. Ft. Myer Drive
Arlington, VA 22209


Itek Corp                                                  1
Attn: Mr Edward Gallet
Optical Sciences Division
10 Maquire Road
Lexington, MA 02173

Perkin Elmer Corp                                          1
Attn: Mr. H. Levenstein
Electro Optical Division
Main Avenue
Norwalk, CT 06856

Hughes Aircraft Company                                    1
Attn: Mr. George Speak
M S. B_156
Culver City, CA 09230


Hughes Aircraft Company                                    1
Attn: Mr. Ken Beale
Centinela Teale Sts
Culver City, CA 90230


Air Force Flight Dynamics Lab                              1
Attn+ Dr. Lynn Rogers
Wright Patterson AFB, OH 45433
```

AFWL/FIBG   1

Attn: Mr. Jerome Pearson
Wright Patterson AFB, OH 45433

Air Force Wright Aero Lab. FIGC   1
Attn. Siva S. Banda
Wright Patterson AFB, OH 45433

Air Force Institute of Technology   1
Attn: Prof. R. Calico/ENY
Wright Patterson AFB OH 45433

Aerospace Corp.   2
Attn: Dr. G.T. Tseng
2350 E. El Segundo Blvd
El Segundo, CA 90245

Aerospace Corp.   1
Attn: Mr. J. Mosich
2350 E. El Segundo Blvd
El Segundo, CA 90245

Aerospace Corp/Bldg 125/1054   1
Attn: Mr. Steve Burrin
Advanced Systems Tech Div.
2400 E El Segundo Blvd
El Segundo, CA 90245

SD/SD/YLVS   1
Attn: Mr. Lawrence Weeks
P O Box 92960
Worldway Postal Center
Los Angeles CA 90009

SD/YCD   1
Attn: YCPT/Capt Gajewski
P O. Box 92960
Worldway Postal Center
Los Angelel, CA 90009

Grumman Aerospace Corp   1
Attn: Dr. A. Mendelson
South Oyster Bay Road
Bethpage, NY 11714

OUSDR&E/DS   1
Attn. Mr. A. Bertapelli
Room 3D136
Pentagon, Washington, DC 20301

Jet Propulsion Laboratory   2
Dr. S. Szermay
4800 Oak Grove Drive
Pasadena, CA 91103

MIT/Lincoln Laboratory   1
Attn: S. Wright
P.O. Box 73
Lexington, MA 02173

MIT/Lincoln Laboratory   1
Attn: Dr. N. Smith
P.O. Box 73
Lexington, MA 02173

Control Dynamics Co.   1
Attn: Dr. Sherman Seltzer
Suite 1414 Executive Plaza
555 Sparkman Drive
Huntsville, AL 35805

Lockheed Space Missile Corp.   5
Attn: A. A. Woods, Jr., O/62-E6
P.O. Box 504
Sunnyvale, California 94088-3504

Lockheed Missiles Space Co.   1
Attn: Mr. Paul Williamson
3251 Hanover St.
Palo Alto, CA 94304

General Dynamics   1
Attn: Ray Halstenberg
Convair Division
5001 Keary Villa Rd
San Diego, CA 92123

STI   1
Attn: Mr. R. C. Stroud
20065 Stevens Creek Blvd.
Cupertiono, CA 95014

NASA Langley Research Ctr   2
Attn: Dr. Earle K. Huckins III
Dr. M. F. Card
Langley Station, Bldg 1293B, MS 230
Hampton, VA 23665

NASA Johnson Space Center   1
Attn: Robert Piland
Ms. EA
Houston, TX 77058

McDonald Douglas Corp   1
Attn: Mr. Read Johnson
Douglas Missile Space Systems Div
5301 Bulsa Ave
Huntington Beach, CA 92607

Integrated Systems Inc.   2
Attn: Dr. N. K. Gupta and M. G. Lyons
151 University Avenue, Suite 400
Palo Alto, California 94301

Boeing Aerospace Company   1
Attn: Mr. Leo Cline
P. O. Box 3999
Seattle, WA 98124
MS 8 W-23

TRW Defense Space Sys Group Inc.   1
Attn: Ralph Iwens
Bldg 82/2054
One Space Park
Redondo Beach, CA 90278

TRW   1
Attn: Mr. Len Pincus
Bldg R-5, Room 2031
Redondo Beach, CA 90278

Department of the NAVY   1
Attn: Dr. K. T. Alfriend
Naval Research Laboratory
Code 7920
Washington, DC 20375

Airesearch Manuf. Co. of Calif.   1
Attn. Mr. Oscar Buchmann
2325 West 190th St.
Torrance, CA 90509

Analytic Decisions, Inc.   1
Attn: Mr. Gary Glaser
1401 Wilson Blv.
Arlington, VA 22209

Ford Aerospace & Communications Corp.   1
Drs. I. P. Leliakov and P. Barba, MS/G80
3939 Fabian way
Palo Alto, California 94304

Center for Analysis   1
Mr. James Justice
13 Corporate Plaza
Newport Beach, CA 92660

W J. Schafer Associates   1
Dr. R. Kappesser
Suite 800
1901 Fort Meyer Drive
Arlington, VA 22209

General Research Corp   1
Attn: Mr. Thomas Zakrzewski
7655 Old Springhouse Road
McLean, VA 22101

Air Force Weapons Laboratory   2
Attn: Capt Terry Hinnerichs
ARAA
Kirtland AFB, NM 87117

Carman Sciences Corp.   1
Attn: Dr. Walter E. Ware
1500 Garden of the Gods Road
P.O. Box 7463
Colorado Springs, CO 80933

MRJ, Inc.   1
10400 Eaton Place
Suite 300
Fairfax, VA 22030

Photon Research Associates   1
Mr. James Myer
P O. Box 1318
La Jolla, CA 92038

Rockwell International   1
Attn: Russell Loftman (Space Systems Group)
(Mail Code - SL56)
12214 Lakewood Blvd.
Downey, CA 90241

Science Applications, Inc.   1
Attn: Mr. Richard Ryan
3 Preston Court
Bedford, MA 01730

U. S. Army Missile Command   1
Attn: DRSMI-RAS/Mr. Fred Haak
Redstone Arsenal, AL

Naval Electronic Systems Command   1
Attn: Mr. Charles Good
PME_106-4
National Center I
Washington, DC 20360

Lockheed Palo Alto Research Laboratory   2
Attn: Dr. J. N. Aubrun, 0/52-56
3251 Hanover Street
Palo Alto, California 94304-1187

U. S. Army/DARCOM   1
Attn: Mr. Bernie Chasnov
AMC Bldg
5001 Eisenhower Ave
Alexandria, VA 22333

Defense Documentation Center   1
Cameron Station
Alexandria, VA 22314

Honeywell Inc.   2
Attn: Dr. Thomas B. Cunningham
Attn: Dr. Michael F. Barrett
2600 Ridgway Parkway MN 17-2375
Minneapolis, MN 55413

NASA Marshal Space Flight Center   2
Attn. Dr. J. C. Blair, ED01
Henry B. Waites
Marshal Space Flight Center, AL 35812

```
TRW                                                      1
Attn: Robert Benhabib
Bldg 82/2024
One Space Park
Redondo Beach, CA 90278

NASA Langley Research Center                             1
Attn: Dr. L. Pinson
MS - 230
Hampton, VA 23665



H. R. Textron                                            1
Attn. Mr. Richard Quartararo
2485 McCabe Way
Irvine,. CA 92714



Naval Research Lab                                       1
Attn: W. Bennett
Mail Code: 7926
Washington, DC 20375
```

TOTAL COPIES REQUIRED   100

Engineer/LCN Signature _Richard M Carman_ 27 Oct 83

MISSION
of
Rome Air Development Center

RADC plans and executes research, development, test and selected acquisition programs in support of Command, Control Communications and Intelligence (C^3I) activities. Technical and engineering support within areas of technical competence is provided to ESD Program Offices (POs) and other ESD elements. The principal technical mission areas are communications, electromagnetic guidance and control, surveillance of ground and aerospace objects, intelligence data collection and handling, information system technology, ionospheric propagation, solid state sciences, microwave physics and electronic reliability, maintainability and compatibility.